

Demonstrating Device-Free Localization based on Radio Tomographic Imaging through Simulations and Experimentation

by

Pranay Sood

A Thesis Submitted to
The Hong Kong University of Science and Technology
In Partial Fulfillment of the Requirements for
The Degree of Master of Philosophy
In the Department of Electronic and Computer Engineering

August 2020, Hong Kong

Authorization

I hereby declare that I am the sole author of the thesis.

I authorize the Hong Kong University of Science and Technology to lend this thesis to other institutions or individuals for the purpose of scholarly research.

I further authorize the Hong Kong University of Science and Technology to reproduce the thesis by photocopying or by other means, in total or in part, at the request of other institutions or individuals for the purpose of scholarly research.



Pranay Sood

August 2020

Demonstrating Device-Free Localization based on Radio Tomographic Imaging through Simulations and Experimentation

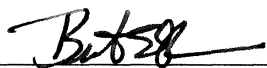
by

Pranay Sood

This is to certify that I have examined the above M.Phil. thesis
and have found that it is complete and satisfactory in all respects,
and that any and all revisions required by
the thesis examination committee have been made.



Prof. Ross Murch, Thesis Supervisor



Prof. Bertram Emil Shi, Head of Department

Thesis Examination Committee

- | | |
|---|---|
| 1. Prof. Daniel Perez Palomar (Chairperson) | Department of Electronic and Computer Engineering |
| 2. Prof. Ross Murch (Supervisor) | Department of Electronic and Computer Engineering |
| 3. Prof. Frankie Chiu | Department of Electronic and Computer Engineering |

Department of Electronic and Computer Engineering
August 2020

ACKNOWLEDGMENTS

I would like to thank my wonderful thesis supervisor Prof. Ross Murch for his invaluable guidance, advice and support for both my personal and academic life. I remember taking the course ELEC 1200 – A System View of Communications: from Signals to Packets with Prof. Ross Murch during my undergraduate studies and it really piqued my interest in the mathematics behind signals and system. I also had the opportunity to work with Prof. Ross Murch for my Final Year Project as an undergraduate student which I really enjoyed and was instrumental in my decision to pursue MPhil under his able guidance.

I found the transition from my undergraduate studies to the MPhil programme quite challenging, especially my first year as I dealt with the demands of adapting to the research lifestyle and was not always on top of my tasks and priorities. In retrospect, my progress in my first year was not very satisfactory and I decided that I wanted to switch gears in my second year. From that point on, I was more motivated to learn and explore new research concepts, ideas, and knowledge and incorporate them into my own research. The feedback and criticism from Prof. Ross Murch was very insightful and encouraged me to bring different approaches and tactics to build on my research skills. If I ever had any doubts in my research, needed career advice, had any personal issues, or needed a little push, Prof. Ross Murch was always there to guide me to the right path with his adept mentorship. Even though it feels as if the two years of my MPhil have flown by very quickly, I was able to explore many facets of research-work during this time; from performing experiments based on the theories learned from books and papers, to writing conference papers and finally, this thesis. This experience has undoubtedly made me more confident and assured as a researcher. Needless to say, this would not have been possible if it was not for Prof. Ross Murch as he has been an incredible advisor and mentor throughout my exceptional MPhil journey.

I also owe my deepest gratitude to my research group members Amartansh Dubey and Jehiel Santos. Amartansh is a very knowledgeable, creative, and brilliant researcher and working with him on this research project has been an amazing experience. I really enjoyed our meeting sessions and his openness to share his insights made our discussions fruitful and rewarding. In addition,

conducting experiments with Jehiel was very memorable as he is a very organised and affable individual. The collaboration with Amartansh and Jehiel played a crucial role in ensuring the success of my experimentation and analysis as well as further enhanced my understanding of Radio Tomographic Imaging and optimization techniques. Not only did I share this experience with brilliant group members, I was also able to make great friends in the process. I want to express my deepest gratitude to my parents, Harsh Sood and Nivedita Sood, and my sister, Aditi Sood, for their love, support, encouragement, and guidance throughout all these years in my academic and personal decisions. Without them, I would not have been able to achieve any of the milestones and personal goals that I had set for myself when I started this journey. I would also like to thank my friends from HKUST and high school for the wonderful times I have shared with them. I am grateful for all the personal and academic discussions we have had together over the years.

Since I have done both my undergraduate and postgraduate studies at HKUST, I have been able to do numerous incredible courses with many exceptional professors. In particular, I would like to thank Prof. Shenghui Song, Prof. Matthew McKay and Prof. Daniel Palomar for offering amazing mathematics and signal processing based courses throughout my studies as well as for being incredible course instructors. I had the wonderful opportunity to also work on some remarkable course projects in the field of Machine and Deep Learning and Random Matrix Theory. In addition, I would also like to thank Prof. Betty Lin for giving me the chance to take courses centred around Technology and Management during my undergraduate studies which encouraged me to explore problems from both technical and business perspectives. I would also like to thank Prof. Pedro Sander, Prof. Ajay Joneja and Prof. Jianan Qu for offering me amazing courses during my undergraduate studies and for being incredible tennis partners. Finally, I am very thankful to Prof. Frankie Chi Yuk Chiu and Prof. Daniel Palomar for agreeing to spare their precious time to be examiners for my thesis.

Lastly, I would like to dedicate this thesis to my family for their endless love, constant support, and all the sacrifices they have made to guide me in getting to where I am today.

TABLE OF CONTENTS

Title Page	i
Authorization Page	ii
Signature Page	iii
Acknowledgments	iv
Table of Contents	vi
List of Figures	viii
Abstract	xii
Chapter 1 Introduction	1
1.1 Objectives	2
1.2 Challenges	2
1.3 Contributions	4
1.4 Thesis Organization	5
1.5 Publication resulting from this Research	6
Chapter 2 The Inverse Scattering Problem	7
2.1 Introduction	7
2.2 The Wave Equation	7
2.3 Approximations to the Scattered Waves	9
2.3.1 Born Approximation	9
2.3.2 Rytov Approximation	10
2.4 Problem Formulation	11
2.5 Through-Wall Imaging	12
2.5.1 Simulations of Born and Rytov Approximations	13

2.6 Limitations and Straight Ray Approximation	13
2.7 Review of Alternative Approaches	14
2.7.1 Visual Sensor Networks	14
2.7.2 RadioBOT	15
2.7.3 Fingerprint-based Localization	15
Chapter 3 Radio Tomographic Imaging	33
3.1 Model	33
3.1.1 Linear Formulation	33
3.1.2 Weight Model	36
3.2 Image Reconstruction	37
3.2.1 Simulation Setup	37
3.2.2 Ill-Posed Inverse Problem and Simulation Results	39
Chapter 4 Experimental Setup and Results	47
4.1 Multiple Wi-Fi Node Measurement System	47
4.1.1 Design of the System	47
4.1.2 Hardware Details	48
4.1.3 Details about the Directional Antenna	48
4.2 Experiment Setup and Tasks	51
4.2.1 System Setup	51
4.2.2 Experimental Tasks and Procedures	53
4.3 Two-Ray Ground-Reflection Model	54
4.4 Experimentation Results	56
4.4.1 Results of Experiment One and Two-Ray Ground-Reflection Model Simulations	56
4.4.2 Results of Experiment Two with Different Objects	59
4.4.3 Results from Experiment Three and Imaging Changes within Indoor Environment	60
Chapter 5 Conclusion	65
References	68

LIST OF FIGURES

2.1	Geometry of the Inverse Scattering Problem.	12
2.2	Reconstructions of a 1λ cylinder with a refractive index of 1.001.	17
2.3	Reconstructions of a 1λ cylinder with a refractive index of 1.01.	18
2.4	Reconstructions of a 1λ cylinder with a refractive index of 1.1.	19
2.5	Reconstructions of a 1λ cylinder with a refractive index of 1.2.	20
2.6	Reconstructions of a 2λ cylinder with a refractive index of 1.001.	21
2.7	Reconstructions of a 2λ cylinder with a refractive index of 1.01.	22
2.8	Reconstructions of a 2λ cylinder with a refractive index of 1.1.	23
2.9	Reconstructions of a 2λ cylinder with a refractive index of 1.2.	24
2.10	Reconstructions of a 4λ cylinder with a refractive index of 1.001.	25
2.11	Reconstructions of a 4λ cylinder with a refractive index of 1.01.	26
2.12	Reconstructions of a 4λ cylinder with a refractive index of 1.1.	27
2.13	Reconstructions of a 4λ cylinder with a refractive index of 1.2.	28
2.14	Reconstructions of a 10λ cylinder with a refractive index of 1.001.	29
2.15	Reconstructions of a 10λ cylinder with a refractive index of 1.01.	30
2.16	Reconstructions of a 10λ cylinder with a refractive index of 1.1.	31
2.17	Reconstructions of a 10λ cylinder with a refractive index of 1.2.	32
3.1	This is an illustration of the RTI network whereby each node is continuously transmitting and receiving signals to one another thus developing many projects that can be utilized to reconstruct an image of physical objects inside the WSNs.	34
3.2	This is an illustration of a single link present in a RTI network which travels in a direct LOS path. The presence of an physical objects causes the signal to be shadowed as it crosses the area of the network in a particular path. The pixels that have been darkened represent the areas of the image where there is a nonzero weighting for that particular link.	35
3.3	Arrangement of the Wi-Fi sensor nodes in a two-dimensional cross-section of a room with dimensions of 3 m by 3 m.	38
3.4	Cylinder with a radius of 0.3 m with the center positioned at (2, 2) and the permittivities being arbitrary.	39

3.5	RTI reconstruction of cylinder using the least-squared-error approach with radius of 0.3 m, permittivity of 1.5 and pixel size of 1.	40
3.6	RTI reconstruction of cylinder using the least-squared-error approach with radius of 0.3 m, permittivity of 3 and pixel size of 1.	40
3.7	RTI reconstruction of cylinder using the least-squared-error approach with radius of 0.3 m, permittivity of 30 and pixel size of 1.	41
3.8	RTI reconstruction of cylinder using the least-squared-error approach with radius of 0.3 m, permittivity of 1.5 and pixel size of 0.5.	42
3.9	RTI reconstruction of cylinder using the least-squared-error approach with radius of 0.3 m, permittivity of 3 and pixel size of 0.5.	42
3.10	RTI reconstruction of cylinder using the least-squared-error approach with radius of 0.3 m, permittivity of 30 and pixel size of 0.5.	43
3.11	RTI reconstruction of cylinder using the least-squared-error approach with radius of 0.3 m, permittivity of 1.5 and pixel size of 0.25.	44
3.12	RTI reconstruction of cylinder using the least-squared-error approach with radius of 0.3 m, permittivity of 3 and pixel size of 0.25.	44
3.13	RTI reconstruction of cylinder using the least-squared-error approach with radius of 0.3 m, permittivity of 30 and pixel size of 0.25.	44
3.14	RTI reconstruction of cylinder using the total variation-based regularization approach with radius of 0.3 m, permittivity of 1.5 and pixel size of 0.1.	45
3.15	RTI reconstruction of cylinder using the total variation-based regularization approach with radius of 0.3 m, permittivity of 3 and pixel size of 0.1.	45
3.16	RTI reconstruction of cylinder using the total variation-based regularization approach with radius of 0.3 m, permittivity of 30 and pixel size of 0.1.	45
3.17	RTI reconstruction of cylinder using the total variation-based regularization approach with radius of 0.3 m, permittivity of 1.5 and pixel size of 0.05.	46
3.18	RTI reconstruction of cylinder using the total variation-based regularization approach with radius of 0.3 m, permittivity of 3 and pixel size of 0.05.	46
3.19	RTI reconstruction of cylinder using the total variation-based regularization approach with radius of 0.3 m, permittivity of 30 and pixel size of 0.05.	46
4.1	Electromechanical fixture between SparkFun ESP32 Thing Board and Directional Antenna.	48
4.2	Measurement gain of the directional antenna at different frequencies.	49
4.3	Radiation pattern of directional antenna at different plane positions of $\phi = 0$, $\phi = 90$ and $\theta = 0$.	50

4.4	Block diagram of the Wi-Fi Node Measurement System.	51
4.5	Two ESP32 boards placed apart from each other.	53
4.6	20 ESP32 boards placed around the surrounding of a 3 m by 3 m region.	55
4.7	Two-ray ground-reflection model.	56
4.8	Mean RSSI obtained between two ESP32 boards placed apart from each other at an increment of 0.5 m. Four trials were performed across multiple days.	57
4.9	Standard deviation of the RSSI obtained between two ESP32 boards placed apart from each other at an increment of 0.5 m. Four trials were performed across multiple days.	57
4.10	Simulation of two-ray ground-reflection model with consideration of directional antenna directivity and wide range of reflection coefficient R .	58
4.11	Comparison of the simulation of the two-ray ground-reflection model with the mean RSSI results of experiment one from the different trials performed.	58
4.12	Wooden table placed between two ESP32 boards.	59
4.13	Result obtained by placing wooden table between two ESP32 boards.	59
4.14	One human placed between two ESP32 boards.	60
4.15	Result obtained by placing one and two humans between two ESP32 boards.	60
4.16	RSSI readings between two ESP32 boards numbered 6 and 13. This image shows both situation where board number 6 acts as a transmitter and board numbered 13 acts as a receiver and vice versa.	61
4.17	Sample of a mode matrix of the RSSI data when there is a presence of one human in the 3 m by 3 m region in the indoor environment.	62
4.18	One human present in a 3 m by 3 m region in the indoor environment at the coordinate of (1.2, 1.2).	62
4.19	Image reconstruction of one human with the localization position being at coordinate of (1.2, 1.2).	62
4.20	Two humans present in a 3 m by 3 m region in the indoor environment with human one being at coordinate (0.6, 1.8) and human two being at coordinate (1.8, 1.2).	63
4.21	Image reconstruction of two human with the localization position of human one being at coordinate of (0.6, 1.8) and human two being at coordinate (1.8, 1.2).	63
4.22	One human present in a 3 m by 3 m region in the indoor environment at the coordinate of (1.2, 1.2).	64
4.23	Image reconstruction of one human with the localization position being at coordinate of (1.2, 1.2) with the implementation of the improved RTI model.	64

- 4.24 Two humans present in a 3 m by 3 m region in the indoor environment with human one being at coordinate (1.2, 1.2) and human two being at coordinate (2.4, 1.8). 64
- 4.25 Image reconstruction of two human with the localization position of human one being at coordinate of (1.2, 1.2) and human two being at coordinate (2.4, 1.8) with the implementation of the improved RTI model. 64

Demonstrating Device-Free Localization based on Radio Tomographic Imaging through Simulations and Experimentation

by

Pranay Sood

Department of Electronic and Computer Engineering
The Hong Kong University of Science and Technology

ABSTRACT

Location Based Services (LBSs) have led to an increase in demand for Device-Free Localization (DFL) in the indoor environment. Radio Tomographic Imaging (RTI) is one well-known localization algorithm that can estimate the position of a physical object on the basis of the received signal strength indicator (RSSI) changes in the environment that are acquired by Wi-Fi or Wireless Sensor Networks (WSNs). This thesis makes two significant contributions. The first contribution involves the demonstration of the RTI approach by utilizing full electromagnetic simulations of an indoor environment. In particular, we considered dielectric cylinders with varying permittivities but fixed radius in which 20 Wi-Fi nodes are deployed on the perimeter (3 m by 3 m) of a region to perform RTI. The RTI approach is based on the line-of-sight (LOS) weighting model with total variation-based regularization which is used to reconstruct and localize the position of the cylinder at high resolution.

The second contribution of the thesis is to utilize the knowledge and fundamentals from the simulations to develop an experimental setup by using inexpensive Wi-Fi hardware modules with directional antenna. We performed experiments on the Wi-Fi hardware modules itself by comparing the mean RSSI of two Wi-Fi hardware modules with the two-ray ground-reflection model at incremental distances in order to explore the impact of multipath fading from the ground and its reflection coefficient. We also introduced a physical object between two Wi-Fi hardware modules to observe the interference caused on the Wi-Fi signal and changes in the RSSI measurements. Finally, we developed a domain of interest identical to the simulations and placed physical objects in the region at different coordinates in order to reconstruct its image and localize its position.

Through both the simulations and experimentation, the RTI methodology is suitable for reconstructing and localizing objects with high permittivity such as humans in the domain of interest. However, RTI tends to face issues with reconstructing images and localizing physical objects with lower permittivities thus motivating further future investigations.

CHAPTER 1

INTRODUCTION

Advancements in wireless communication have resulted in the emergence of Location Based Services (LBSs) and these have become essential for users to make decisions or plan activities. LBSs have a wide range of applications in the area of smart transportation, healthcare, households, etc [1]. Global Positioning System (GPS) is able to provide essential location and time information to the users. However, it has poor accuracy in indoor environments due to signal degradation when passing through walls and buildings. Furthermore, in certain special applications such as security monitoring, intrusion detection, emergency rescue, etc., [2] it is not possible to equip the target with GPS devices. Therefore, Device-Free Localization (DFL) is an emerging technology that overcomes the issue of equipping the target with the wireless transceiver device. DFL techniques can detect and locate a human or an object by measuring received signal strength indicator (RSSI) changes in the environment through the implementation of Wi-Fi or Wireless Sensor Networks (WSNs) [3].

Radio Tomographic Imaging (RTI) is a technique that can perform DFL using image reconstruction for localization. The concept of RTI is very similar to X-Ray tomography, whereby the projections of the object are generated through the use of rays that pass through the object in order to obtain the attenuation based on the size and permittivity of that object [4]. RTI is able to reconstruct or image the attenuation due to objects using the shadowing losses measured at sensors in the WSNs. This algorithm is suitable for indoor applications because the induced reflection created by the objects develop a strong non-linear attenuation field map [5]. The deployment of WSNs in a monitoring area makes it possible to establish wireless links between each sensor that continuously send packets of information to the other sensors to obtain RSSI [6]. As a result, RTI can detect objects such as the human body and furniture [2]. Therefore, when an object enters in a region with WSNs, radio-frequency (RF) signals pass through the object thus resulting in shadowing losses and change in RSSI of the sensor links [7].

In contrast to traditional localization techniques that the tracked entities are required to carry radio devices such as radio frequency identification (RFID) tag, DFL can localize the target without attaching any electronic device and does not require the target to cooperate with the localization system. In some applications, such as battlefield surveillance, emergency rescue, and security safeguard, it is impractical to require a target to carry a cooperative device. Under the situations that traditional localization systems do not work, RSSI based DFL can still infer the target's location by measuring the target's effect on the RSSI of the network's links and becomes an effective method for passive localization

1.1 Objectives

Given the background of DFL and RTI, the following objectives that have been set for the thesis:

1. Develop an understanding of the Inverse Scattering Problem in order to understand the different types of approximation implemented in reconstructing the object with ranges in their size and refractive index.
2. Demonstrate DFL using RTI by using exact electromagnetic simulations. Within the simulation, we use cylinders with arbitrary size and permittivities and through the RTI reconstruction methodology, we are able to localize the position of the cylinder.
3. Discuss and provide details of the indoor environment experimentation along with performing a wide range of experimental tests and configurations on the hardware that is being utilized.

1.2 Challenges

DFL is also a difficult and challenging process because it relies on the underlying physics of radio propagation. Whenever dealing with the transmission and receiving of radio signals like Wi-Fi signal, it is important to consider that in a wireless medium, the power of the propagating receiving signal is affected by path loss, shadowing and multipath fading. Path loss occurs when there is

reduction in the power of the receiving signal due to the distance between the transmission and receiving antenna as the electromagnetic wave propagates through space meanwhile, shadowing is the variation in the attenuation in the signal when there is a presence of an obstacle thus causing the signal to be absorbed, scattered or diffracted. Finally, multipath fading is when the signals are received by the antenna from two or more paths. In the case of our research, we have considered path loss via the free-space path loss and shadowing allows us to obtain the attenuation caused by the presence of a physical object in the indoor environment and this allows us to perform the localization and reconstruction of that object. In the case of multipath fading, we have examined the two-ray ground-reflection model to understand the impact of the reflection from the ground when performing the experiment. However, it is simply not just the ground from which the receiving signal is being measured. When performing an experiment in an indoor environment, other areas of the room such as the ceiling, walls and other objects that are present outside the domain of interest may have an impact on the RSSI of the received signal and it is quite challenging to identify what could be causing the issue. Prior to using directional antennas, we were simply just using the hardware modules with its in-built omnidirectional antenna to obtain the readings and it was very difficult and problematic due to the inconsistency in readings across different trials due to the effect of multipath fading. As a result, to minimize the impact multipath fading, directional antennas were attached to the ESP32 boards in order to obtain more consistent readings.

Another major challenge with the experimentation are that we are simply examining the magnitude when performing the 2D reconstruction of physical object and not examining the change in the phase on the Wi-Fi signals. This is quite difficult with the current hardware modules that we are using as it only restricted to measuring the change in RSSI.

Since the aim of this study is to perform reconstruction and localize the position of physical objects by detecting the change in the RSSI in an indoor environment, we can identify this procedure as an inverse problem. This is because in both the simulations and experimentation, we have considered the situation of a finite number of hardware modules that are transmitting and receiving Wi-Fi signals. The presence of an object will cause the Wi-Fi signal to attenuate thus resulting in the change in RSSI that is being measured. Given that we have the change in the RSSI measured and knowledge regarding the representation of the indoor environment, we want to determine the

change in the attenuation caused by the object present in the domain of interest thus making it an inverse problem. In addition, it is an underdetermined inverse problem as the limitation in data measurement results in higher number of unknowns in comparison to the measurements. Subsequently, given that we have only focused on using 20 hardware modules for measurements of the results, we are faced with the issue of having less information due to the presence of less data and this makes 2D imaging quite challenging as we have to utilize mathematical optimization tools and methodology in order to perform image reconstruction and localization. If more hardware modules could have been implemented, this would make it possible to obtain more data measurements thus making it possible to obtain results at higher resolution.

Finally, the last major challenge is to perform both the experiment and simulations from the 3D perspective as it would require significant computing resources. In addition, while performing the experiments, it is difficult to place the hardware modules on the ceiling of a room to obtain the results. Therefore, we have made the assumption of placing the hardware modules in a domain of interest from a 2D perspective and the implementation of directive antennas will ensure that there will be less reflections from the ceiling.

1.3 Contributions

To meet the challenges and objectives, two major contributions have been performed in fully understanding and improving the line-of-sight (LOS) based RTI models. The first major contribution has been the demonstration of RTI by using exact electromagnetic simulations. To our knowledge, this has not been performed previously due to the electrical size (in wavelengths) of the problem. In order to overcome the large computational requirement, we have decided to implement straightforward exact electromagnetic formulation based on the summation of an eigenfunction expansion of the electromagnetic field. As a result, this has allowed us develop simulations of cylinders with wide range of sizes and permittivities thus allowing us to test the RTI methodology in order to examine the image reconstructed and its ability to localize the position of the cylinder. In addition, the least-squared-error approach has been used in [7] and in order to perform localization at a even higher resolution with smaller grid size, we have decided to implement the total variation-based

regularization which is a significant improvement on the least-squared-error approach.

The second contribution that we have done is performing experiments in order to provide validation of the methodology implemented when performing the simulations. The experimentation scope has already been explored by Mostofi [8] whereby robots with highly directional antennas were implemented to receive the signals with minimal scattered signal. It was a significant improvement in the performance of LOS based RTI model but this procedure requires large amount of data and it is not a cost effective method. Furthermore, it does not fall into the scope of WSNs and not very practical also. As a result, we have decided to implement hardware modules with directional antennas that are inexpensive and equally as effective. We have performed different types of experiments on the hardware modules and compared the experimental results with theoretical models like two-ray ground-reflection model to examine the performance of the hardware modules. In addition, we have recorded measurements to examine the interference caused by the presence of different physical objects with different permittivities along with performing image reconstruction and localization.

Finally, since LOS based RTI model uses the magnitude measurement and ignores the presence of phases, we have decided to also explore inverse scattering for imaging whereby both magnitude and phase measurements are taken in account. We decided to examine both the Born and Rytov approximation and the impact of the size and refractive index of an object when using these approximations as means of reconstruction.

1.4 Thesis Organization

The remainder of the thesis is organised as follows. In order to accomplish the set objectives of this thesis, it is essential to understand the prerequisites of the Inverse Scattering Problem which is introduced in Chapter 2. In addition, a review of alternative approaches to DFL is also provided. Chapter 3 describes the RTI model as discussed by Wilson and Patwari [7] and the total variation-based regularization that we have implemented. It will also focus on the simulation setup along with describing and justifying the results obtained from the setup. Chapter 4 describes the indoor environment experimental setup. This involves a thorough understanding of the hardware modules

that has been implemented for the experiments along with the software side and programming modules that have been designed for data logging, collection and processing. Finally, the results of the experimentation are also displayed and discussed in this chapter. Finally, we conclude in Chapter 5 and discuss future plans.

1.5 Publication resulting from this Research

1. P. Sood, A. Dubey, C. Y. Chiu, and R. Murch, “Demonstrating Device-Free Localization based on Radio Tomographic Imaging,” *IEEE International Symposium of Antennas and Propagation and North American Radio Science Meeting*, 2020.
2. A. Dubey, P. Sood, J. Santos, C. Y. Chiu, and R. Murch, “Imaging Changes in Indoor Environment using Approximate Inverse Scattering Method and Wi-Fi Signals.” In preparation.

CHAPTER 2

THE INVERSE SCATTERING PROBLEM

2.1 Introduction

In order to fully understand the inverse scattering problem, it is essential to understand the fundamentals of imaging three-dimensional (3D) objects into two-dimensional (2D) images. X-Ray computerized tomography (CT) has been the common tool in the field of the medical community to derive 2D diagnostic images. However, there has also been an awareness of dangers that have been caused by the ionizing radiation thus making X-Ray CT unsuitable for mass screening [9]. As a result, other imaging modalities have been explored have been explored with one solution being the theory of inverse scattering known as Diffraction Tomography.

2.2 The Wave Equation

When dealing with the inverse scattering problem in regards to the scalar Helmholtz equation, the algorithm for Diffraction Tomography [10] are derived from the general equation of wave propagation in an inhomogeneous medium. In the homogeneous medium, the general form of a wave equation becomes the Helmholtz equation which is represented as

$$(\nabla^2 + k^2)u(\mathbf{r}) = 0 \quad (2.1)$$

where $u(\mathbf{r})$ represents the scattered field. Meanwhile, k represents the wave number which depends on the properties of the medium and scattered field. In the inhomogeneous Helmholtz case, equation (2.1) can be written

$$(\nabla^2 + k^2)u(\mathbf{r}) = -f(\mathbf{r})u(\mathbf{r}) \quad (2.2)$$

whereby $f(\mathbf{r})$ is the scattering potential [11] and the function of deviations of medium [9]. In the acoustic case, the first order approximations of the expression $f(\mathbf{r})$ is given by

$$f(\mathbf{r}) = k^2(n(\mathbf{r}) - 1) \quad (2.3)$$

where $n(\mathbf{r})$ is the refractive index of each particular point of the object. If we were to ignore the effect of polarization, the function of $f(\mathbf{r})$ in the electromagnetic case is expressed as

$$f(\mathbf{r}) = 2k^2(n(\mathbf{r}) - 1) \quad (2.4)$$

whereby $n(\mathbf{r})$ is

$$n(\mathbf{r}) = \sqrt{\frac{\mu(\mathbf{r})\epsilon(\mathbf{r})}{\mu_0\epsilon_0}} \quad (2.5)$$

In equation (2.5), μ represents the magnetic permeability and ϵ represents the dielectric constant and the subscript of zero is to indicate their average values [9]. To deal with the inhomogeneity of $f(\mathbf{r})$, we make use of the Green's function $G(\mathbf{r} - \mathbf{r}')$. Green's function is considered as an impulse response of an inhomogeneous Helmholtz equation with specified initial or boundary conditions [11]. Since the scalar Helmholtz equation (2.2) cannot be solved directly, a solution can be written directly in terms of Green's function as

$$(\nabla^2 + k^2)G(\mathbf{r} - \mathbf{r}') = -\delta(\mathbf{r} - \mathbf{r}') \quad (2.6)$$

$$G(\mathbf{r} - \mathbf{r}') = \frac{\exp(jk|\mathbf{r} - \mathbf{r}'|)}{4\pi|\mathbf{r} - \mathbf{r}'|} \quad (2.7)$$

Here, $\delta(\mathbf{r} - \mathbf{r}')$ is a Dirac delta function with translational property [11]

$$\int \delta(\mathbf{r} - \mathbf{r}')g(\mathbf{r}')d\mathbf{r}' = g(\mathbf{r}) \quad (2.8)$$

Now we can derive the integral representation of of scattered field $u(\mathbf{r})$ as

$$\begin{aligned} f(\mathbf{r})u(\mathbf{r}) &= \int \delta(\mathbf{r} - \mathbf{r}')f(\mathbf{r}')u(\mathbf{r}')d\mathbf{r}' \\ &= - \int (\nabla^2 + k^2)G(\mathbf{r} - \mathbf{r}')f(\mathbf{r}')u(\mathbf{r}')d\mathbf{r}' \\ &= -(\nabla^2 + k^2) \int G(\mathbf{r} - \mathbf{r}')f(\mathbf{r}')u(\mathbf{r}')d\mathbf{r}' \end{aligned} \quad (2.9)$$

With the comparison of equations (2.2) and (2.9), the scattered field $u(\mathbf{r})$ can we rewritten as

$$u(\mathbf{r}) = \int G(\mathbf{r} - \mathbf{r}')f(\mathbf{r}')u(\mathbf{r}')d\mathbf{r}' \quad (2.10)$$

which is now the integral equation to the inhomogeneous wave equation [11].

2.3 Approximations to the Scattered Waves

Given that it is challenging to solve equation (2.9) for the scattered field, we have to make approximations and this is where we introduce the two types of approximations which are the Born and Rytov approximations. In both of these approximations, the definition of scattered field $u(\mathbf{r})$ is the superposition of the incident plane wave $u_0(\mathbf{r})$ and a scattered component $u_s(\mathbf{r})$ [11].

$$u(\mathbf{r}) = u_0(\mathbf{r}) + u_s(\mathbf{r}) \quad (2.11)$$

2.3.1 Born Approximation

The Born approximation is the simpler approach and the integral of the scattered field can be expressed as

$$u_s(\mathbf{r}) = \int G(\mathbf{r} - \mathbf{r}') f(\mathbf{r}') u_0(\mathbf{r}') d\mathbf{r}' + \int G(\mathbf{r} - \mathbf{r}') f(\mathbf{r}') u_s(\mathbf{r}') d\mathbf{r}' \quad (2.12)$$

but given the scattered field, $u_s(\mathbf{r})$ is relatively small compared to $u_0(\mathbf{r})$, the effects of the second integral in equation (2.12) can be considered negligible in order to arrive to this approximation

$$u_s(\mathbf{r}) \simeq u_B(\mathbf{r}) = \int G(\mathbf{r} - \mathbf{r}') f(\mathbf{r}') u_0(\mathbf{r}') d\mathbf{r}' \quad (2.13)$$

First order Born approximation is considered valid when the magnitude of the scattering is small in comparison to the incident field. Hence, when this is true, the incident field is a close approximation to the total field in the integral equation (2.13) thus showing that one condition for this to be true when the total phase shift in the incident field as it passes through the object must be less than π [9]. Therefore, the higher order approximations of the total field $u(\mathbf{r})$ are possible with the Born approach with the total field represented as

$$u(\mathbf{r}) = u_0(\mathbf{r}) + u_1(\mathbf{r}) + u_2(\mathbf{r}) + \dots \quad (2.14)$$

Therefore, the higher order terms are represented by

$$u_{i+1}(\mathbf{r}) = \int G(\mathbf{r} - \mathbf{r}') f(\mathbf{r}') u_i(\mathbf{r}') d\mathbf{r}' \quad (2.15)$$

2.3.2 Rytov Approximation

Another approximation to the scattered field is known as the Rytov approximation which assumes that the total field can be expressed as complex phase or

$$u(\mathbf{r}) = \exp(\phi(\mathbf{r})) \quad (2.16)$$

Therefore, we can rewrite the wave equation (2.1) as

$$\begin{aligned} (\nabla^2 + k^2)u(\mathbf{r}) &= 0 \\ \nabla[\nabla\phi \exp(\phi)] + k^2 \exp(\phi) &= 0 \\ \nabla^2\phi \exp(\phi) + (\nabla\phi)^2 \exp(\phi) + k^2 \exp(\phi) &= 0 \end{aligned} \quad (2.17)$$

thus obtaining for the inhomogeneous Helmholtz case

$$(\nabla\phi)^2 \exp(\phi) + k^2 \exp(\phi) = -f(\mathbf{r}) \quad (2.18)$$

With the total phase represented as

$$\phi(\mathbf{r}) = \phi_0(\mathbf{r}) + \phi_s(\mathbf{r}) \quad (2.19)$$

By substituting the expression (2.19) for the total field into the inhomogeneous Helmholtz equation (2.2) and simplifying it by subtracting out the effect of the homogeneous solution [9], we find that

$$u_0(\mathbf{r})\phi_s(\mathbf{r}) = \int G(\mathbf{r} - \mathbf{r}')u_0(\mathbf{r}')[(\nabla\phi_s)^2 + f(\mathbf{r}')]d\mathbf{r}' \quad (2.20)$$

In the Rytov solution, it is assumed that the terms in the brackets in equation (2.20) can be approximated to

$$(\nabla\phi_s)^2 + f(\mathbf{r}') \simeq f(\mathbf{r}') \quad (2.21)$$

Therefore, the Rytov solution of the scattered field becomes

$$\phi_s(\mathbf{r}) = \frac{1}{u_0(\mathbf{r})} \int G(\mathbf{r} - \mathbf{r}')u_0(\mathbf{r}')f(\mathbf{r}')d\mathbf{r}' \quad (2.22)$$

or comparison to equation (2.13)

$$\phi_s(\mathbf{r}) = \frac{u_s(\mathbf{r})}{u_0(\mathbf{r})} \quad (2.23)$$

The assumption in Rytov approximation is that $\nabla\phi_s^2$ is small compared to the object function $f(\mathbf{r}')$. This is equivalent to saying that change in the scattered field per unit length must be small. In addition, the Rytov approximation is much more valid under a less restrictive set of conditions in comparison to the Born approximation [9].

2.4 Problem Formulation

After understanding the mathematics behind the fundamentals of the approximation of the scattered waves, it is essential to formulate the inverse scattering problem. The inverse scattering problem is determining the properties of the object through the measurements of the scattered field that are obtained based on a defined incident radiation. Let us consider an environment whereby the transmitted electromagnetic radiation is denoted as E_{Tx} and the received radiation is denoted as $E_{Rx}^{m,b,t}$ with an unknown indoor environment designated as D . Measurement of E_{Rx}^m is referred to as monostatic radar meanwhile, the measurement E_{Rx}^b is known as bistatic radar and if E_{Rx}^t is measured, it can be referred to as diffraction tomography [12]. Fig. 2.1 illustrates the geometry of the Inverse Scattering Problem.

One possible approach to formulate the inverse scattering for an indoor environment is to formulate it as a volume source integral whereby the received field has been characterized at any position $\mathbf{r} \in \mathbb{R}^3$ and it resembles equation (2.10) but from a 3D understanding

$$E_{Rx}(\mathbf{r}) = E_{Tx}(\mathbf{r}) + \iiint_D G(\mathbf{r} - \mathbf{r}') f(\mathbf{r}') u(\mathbf{r}') dV(\mathbf{r}') \quad (2.24)$$

The integration on the RHS of equation (2.24) is a representation of the scattered electromagnetic field that is added to the incident field $E_{Tx}(\mathbf{r})$. In indoor propagation, majority of the work has been focused on finding the material parameter through the total received signal of a receiver $E_{Rx}(\mathbf{r})$. As a result, inverse problem becomes difficult in determining the material parameter $f(\mathbf{r}')$ from $E_{Rx}(\mathbf{r})$ and this is because both $f(\mathbf{r}')$ and total field $E_{Rx}(\mathbf{r})$ are not known inside the indoor environment D with the only information that we know from the outside is D . In order to determine the material $f(\mathbf{r}')$, through-wall imaging is an example of a technique through which the environment can be found immediately from behind the walls.

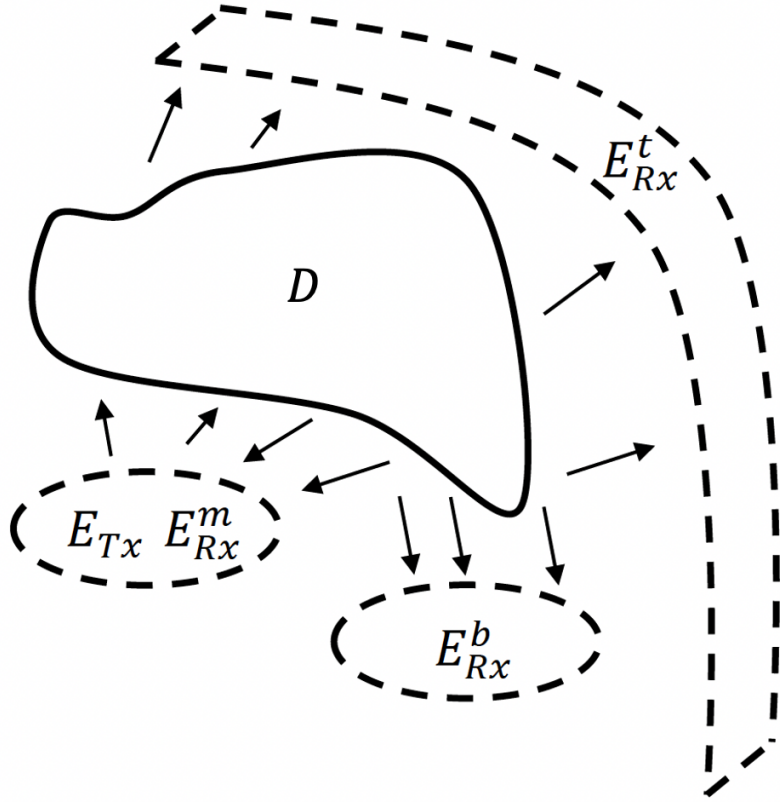


Figure 2.1: Geometry of the Inverse Scattering Problem.

2.5 Through-Wall Imaging

Through-wall imaging is highly based on Born approximation as discussed in section 2.3.1 but now introducing it to the volume source integral. The Born approximation is implicitly assumed to be in monostatic and bistatic radar and therefore, a straightforward relation between the received field and the scattering cross-section of the scatters inside the indoor environment can be obtained [13]. The Born approximation is based on approximating the unknown total integral field in equation (2.24) with the known transmitted field such that the received electromagnetic field is simply denoted as the integral of the material parameters $f(\mathbf{r}')$. Based on our knowledge from equations (2.13) and (2.24), the Born approximation can be denoted as

$$E_{Rx}(\mathbf{r}) = \iiint_D G(\mathbf{r} - \mathbf{r}') f(\mathbf{r}') E_{Tx}(\mathbf{r}') dV(\mathbf{r}') \quad (2.25)$$

in the above expression, $f(\mathbf{r}')$ is now considered as the radar cross section of the objects in the indoor environment [13].

Another possible formulation of through-wall imaging proposed has been on the basis of diffraction tomography [14]. In this particular configuration, the problem is formulated in a tomographic form whereby the transmitted field is related to the transmitted signals that are passing through target area or indoor environment D as shown in Fig. 2.1 and E_{Rx}^t are measured. As a result, Rytov approximation is much more suitable because it is considered more precise and incorporates the effect of scattering of all the objects present in D as a linear model [14]. Using our knowledge from equations (2.22) and (2.24) the Rytov approximation can be formulated as

$$E(\mathbf{r}) = E_{Tx}(\mathbf{r}) \exp(j\phi(\mathbf{r})) \quad (2.26)$$

where

$$\phi(\mathbf{r}) = \frac{-j}{E_{Tx}(\mathbf{r})} \iiint_D G(\mathbf{r} - \mathbf{r}') f(\mathbf{r}') E_{Tx}(\mathbf{r}') dV(\mathbf{r}') \quad (2.27)$$

2.5.1 Simulations of Born and Rytov Approximations

Based on our understanding of the Born and Rytov approximations, simulations were conducted whereby we decided to test both the approximations by using cylinders with different sizes and refractive indexes. Therefore, we have decided to simulate the reconstructions of cylinders with four different radii of 1λ , 2λ , 4λ , and 10λ with four different refractive indexes of 1.001, 1.01, 1.1, and 1.2. Figs. 2.2-2.13 display the simulations that have been conducted with different approximations

2.6 Limitations and Straight Ray Approximation

Based on the simulations from Figs. 2.2-2.13, it can be observed that reconstructions done through Born approximation are quite good at high refractive indexes however, the reconstructions tend to have issues with cylinders with larger radius. This is where Rytov approximation is introduced as it does excellent reconstructions of cylinders with large radius of 4λ and 10λ . Rytov approximation

also works well with the reconstruction of cylinders with small radius however, the downside of Rytov approximation is that it fails at a high refractive index of 1.1 and 1.2. Furthermore, the approximations are being used for reconstructions of cylinders with low refractive indexes but in an indoor environment, we want to reconstruct images of objects that have high refractive indexes, these approximations are suitable and hence, we have to look at other methodologies.

Given these fundamental issues with both these approximations, this is where the straight ray approximation is a suitable methodology that can be implemented for reconstruction purposes. In the straight ray approximation, Wi-Fi signals of 2.4 GHz are utilized with the particular characteristic of travelling in direct path from the transmitter to receiver and thus travelling in the straight line. Hence, it makes it possible to conduct through-wall imaging on the basis of RSSI and this method is highly suitable in detecting changes in the environment when an object of high refractive index and large size is introduced. The following methodology is further explored in Chapter 3.

2.7 Review of Alternative Approaches

In this section, we will provide a revision of the alternative approaches and existing technologies in the field of LBSs.

2.7.1 Visual Sensor Networks

Visual sensor networks such as the implementation of low-power camera nodes has been utilised for DFL and tracking people [15]. However, the issue of using cameras is that an image takes a large amount of memory data, which often becomes a constraint when there is a limitation in network resources. Another major weakness faced by cameras is that image quality tends to deteriorate under poor lighting conditions thus making camera nodes unsuitable in dark indoor environments [16].

To overcome the above-mentioned issues of the camera, visible light communication (VLC) using LEDs has emerged as a new innovative solution for indoor positioning systems [17]. VLC ensures that there is high speed data transfer ensuring a high bandwidth. Furthermore, it is more

accurate and efficient compared to visual sensor nodes. Despite being a very accurate system, the positioning algorithms implemented have been quite complex. This is due to the problem of packet loss caused by interference when there is an overlap in the light beam regions. One such algorithm that has been proposed to overcome the complexity of the VLC system is the multiple LED estimation model (MLEM) [18]. It is a relatively simple positioning algorithm whereby the packets are susceptible to collision [18]. However, the simplicity of the algorithm compromises the speed and efficiency when information of the position needs to be updated.

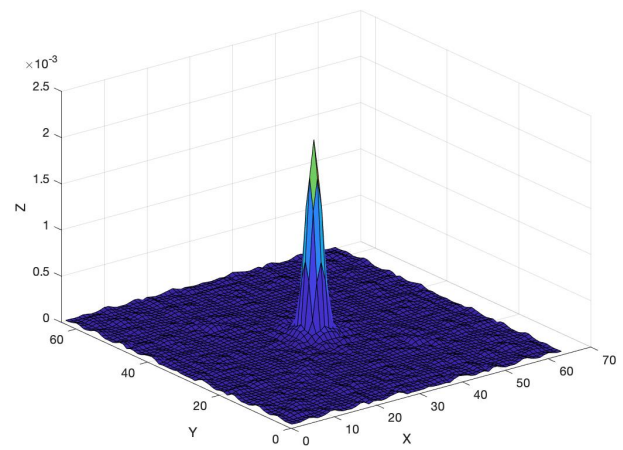
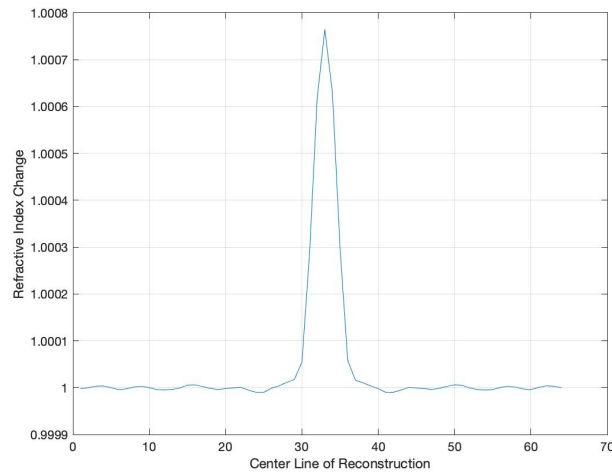
2.7.2 RadioBOT

Instead of using sensor nodes like the above-mentioned methodologies, Mostofi [14] proposed the idea of using two autonomous robots whereby one robot would be transmitting radio signals while the other robot would be receiving the signals and detecting the RSSI. Similarly, RadioBOT was another methodology that was proposed by Georgia Institute of Technology [19]. The system deployed eight individual robots and a central desktop server that transmit and receive radio signals in order to acquire data. The underlying issue with the utilization of autonomous robots is that there is an increase in difficulty and cost when establishing the hardware and software setup for these systems. Despite achieving high performance, these proposed systems are simply not as applicable as using WSNs.

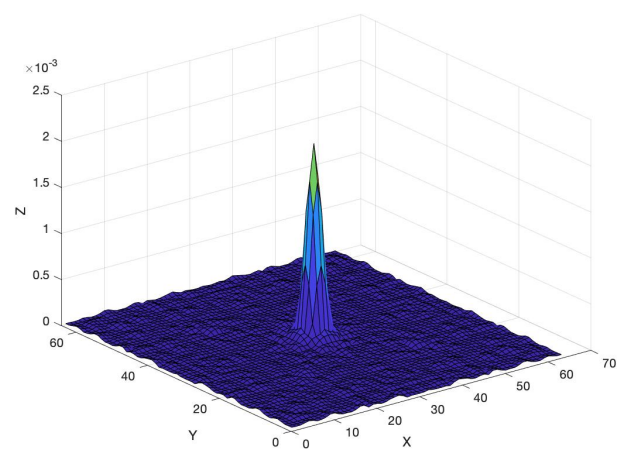
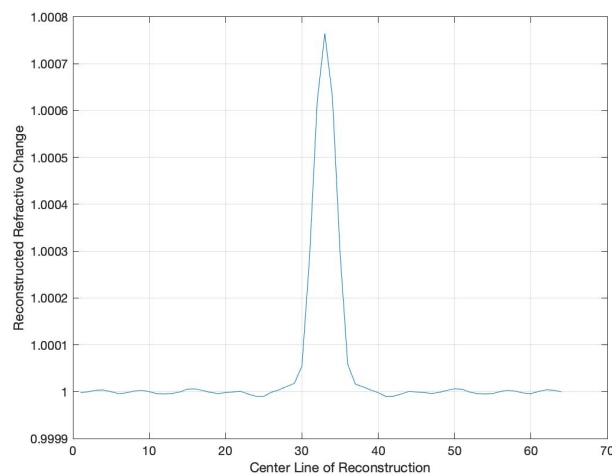
2.7.3 Fingerprint-based Localization

There has been a lot of research conducted on a new approach known as fingerprint-based localization whereby the RSSI is recorded from a wide range of access points and the information is then stored in a database along with the coordinates of the object in an offline phase [3]. During the online tracking phase, the current RSSI of the unknown location is compared to the stored information in the fingerprint and the closest comparison of the match is returned to provide the localization of the object. However, there is a lot of improvement required in terms of accuracy for this methodology because if there is a change in the environment, such as removal or addition of objects or simply a changing from one room to another, there is a change in the "fingerprint" and

hence the database will have to be updated continuously. This is because this approach develops a training model for one particular "fingerprint" and a significant change in the environment can result in inaccurate results [3].

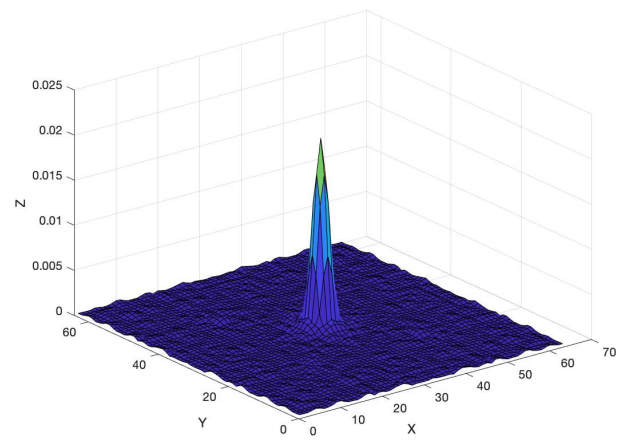
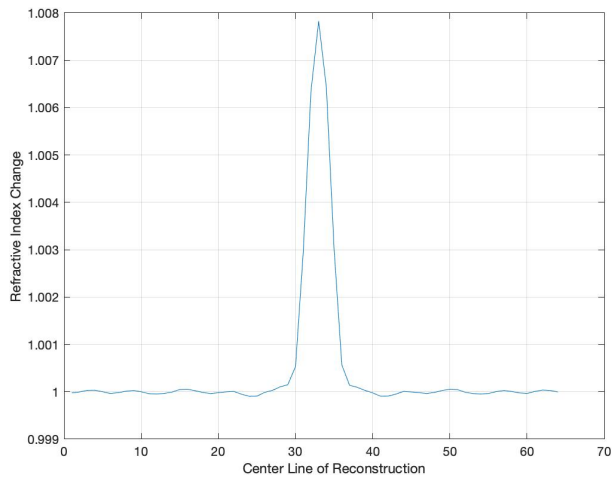


(a) Born Approximation

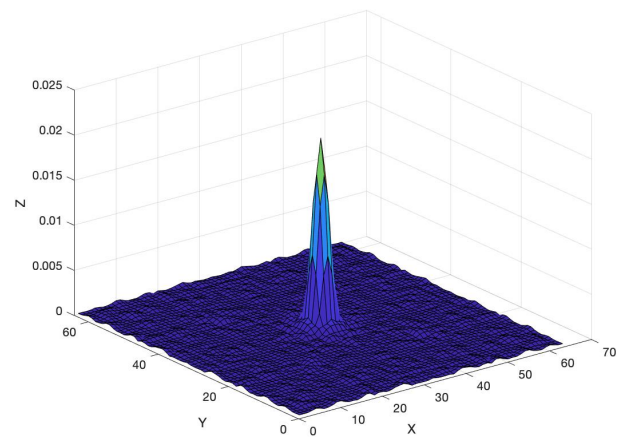
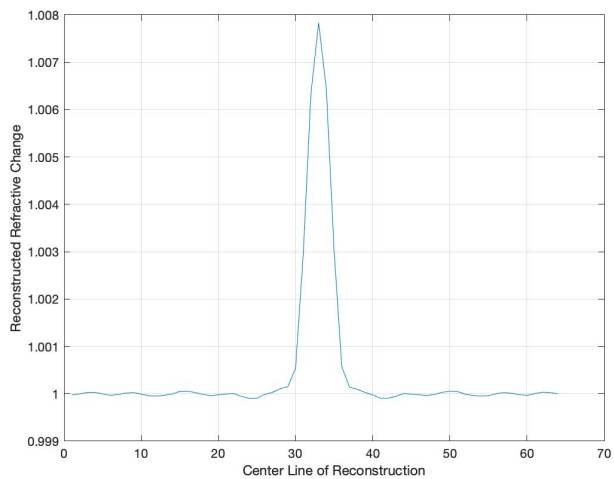


(b) Rytov Approximation

Figure 2.2: Reconstructions of a 1λ cylinder with a refractive index of 1.001.

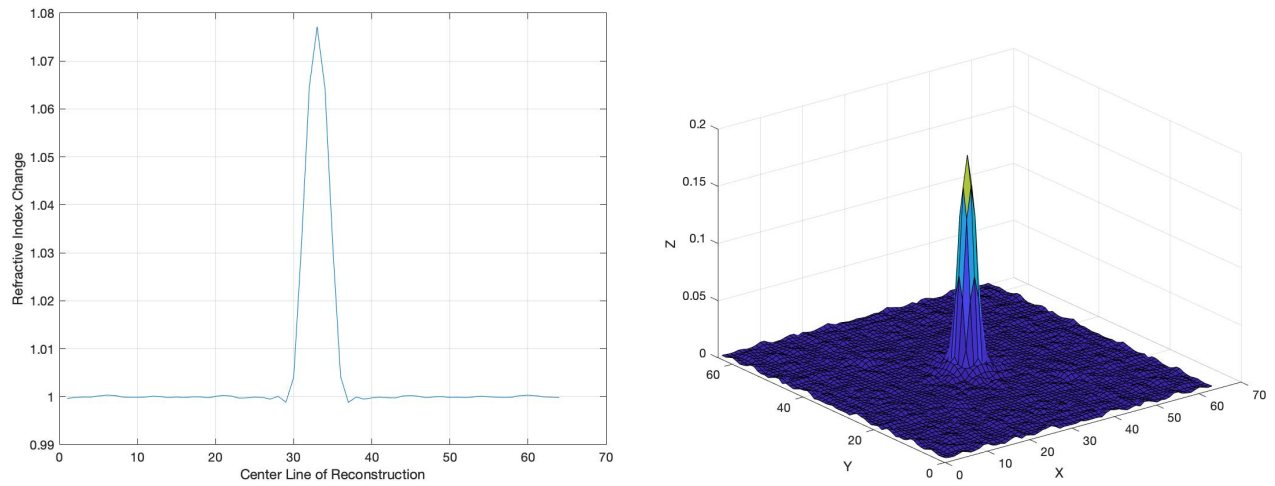


(a) Born Approximation

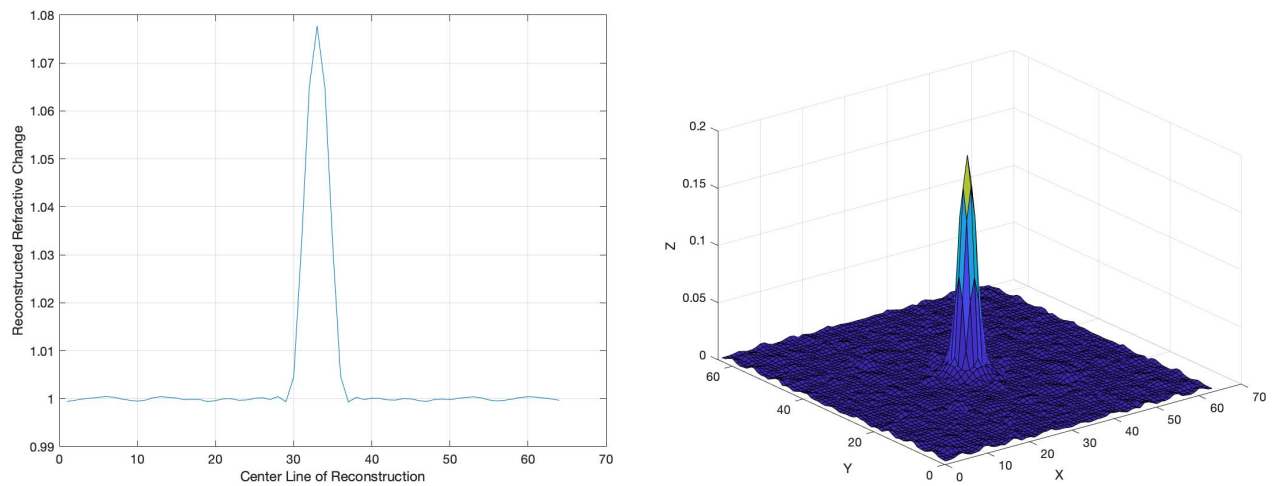


(b) Rytov Approximation

Figure 2.3: Reconstructions of a 1λ cylinder with a refractive index of 1.01.

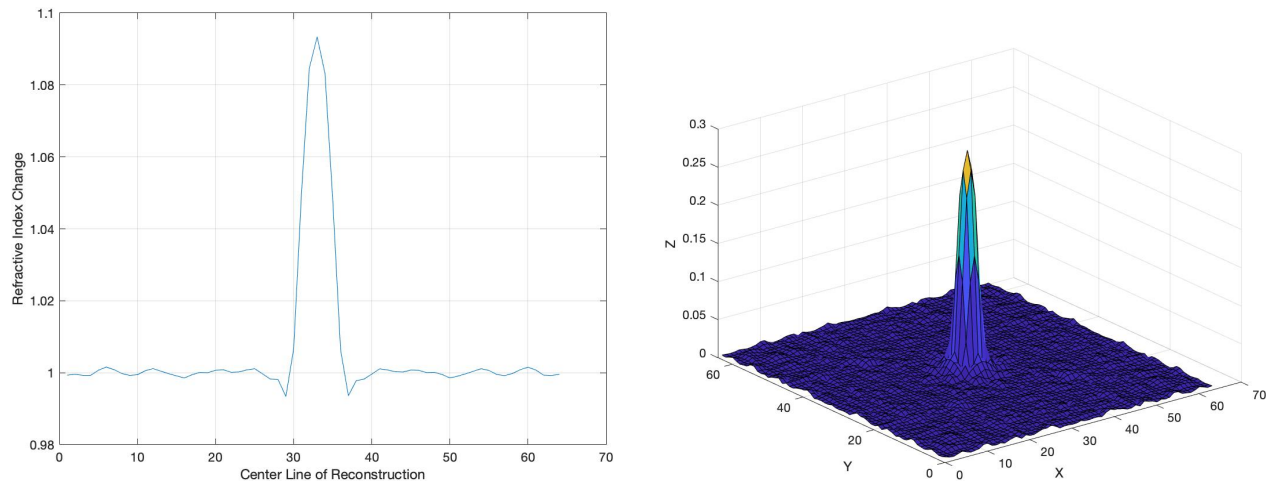


(a) Born Approximation

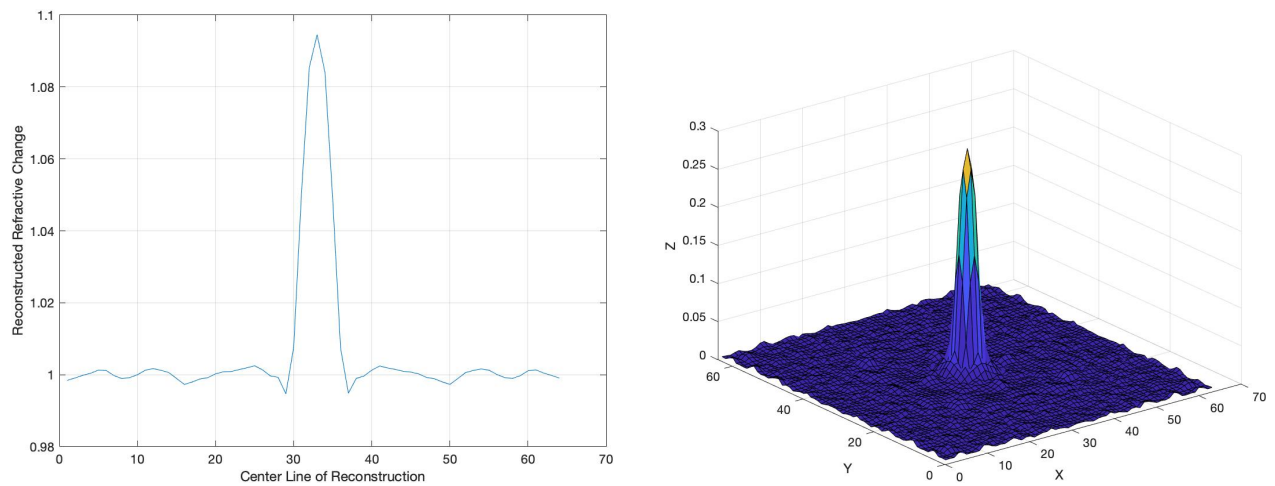


(b) Rytov Approximation

Figure 2.4: Reconstructions of a 1λ cylinder with a refractive index of 1.1.

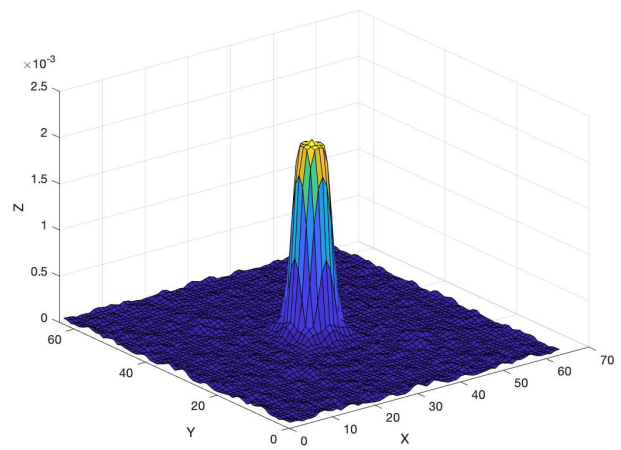
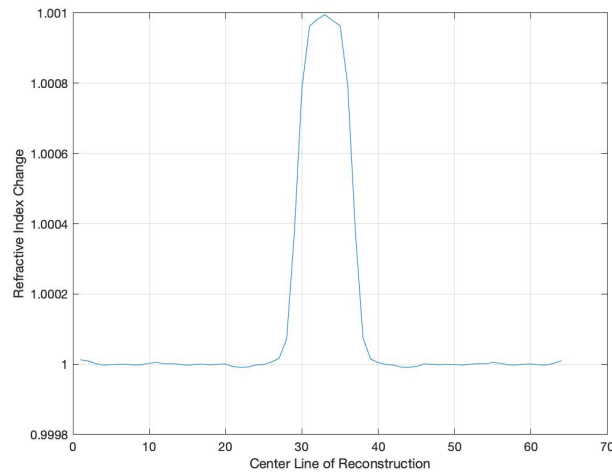


(a) Born Approximation

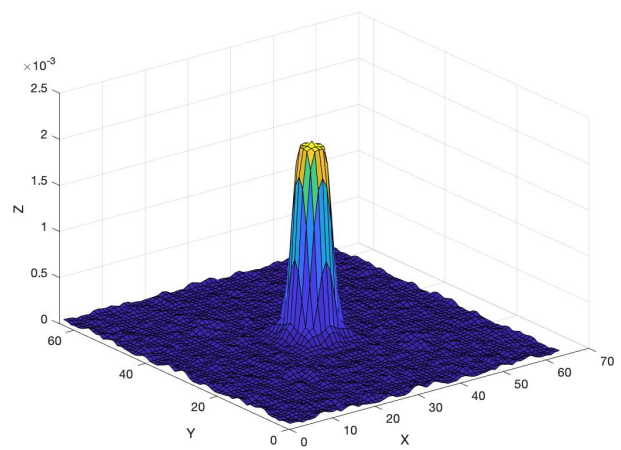
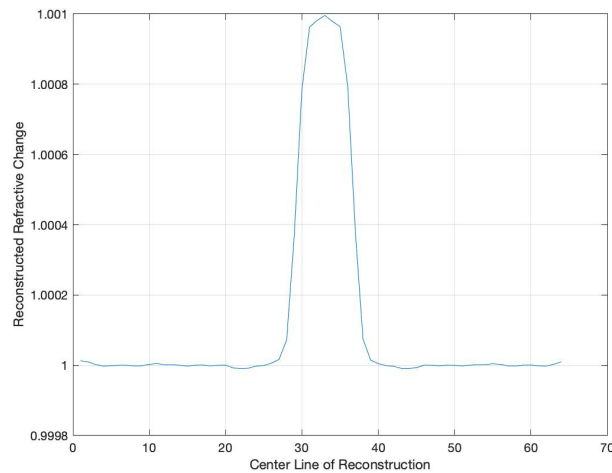


(b) Rytov Approximation

Figure 2.5: Reconstructions of a 1λ cylinder with a refractive index of 1.2.

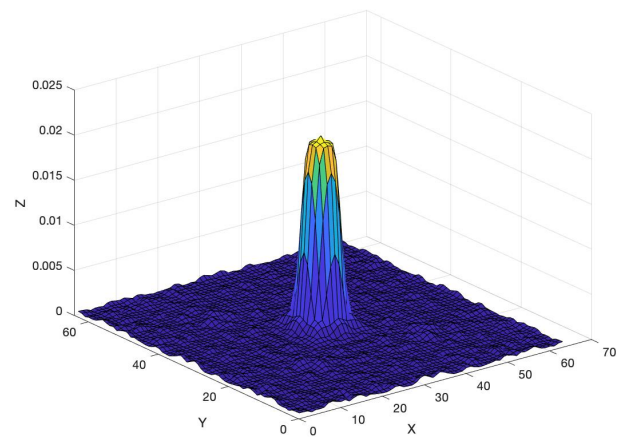
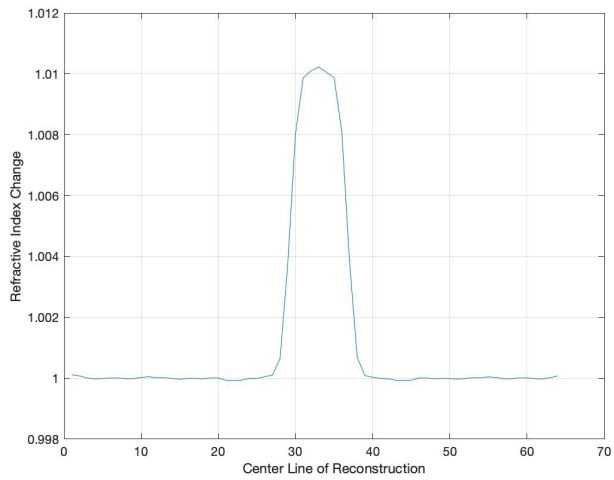


(a) Born Approximation

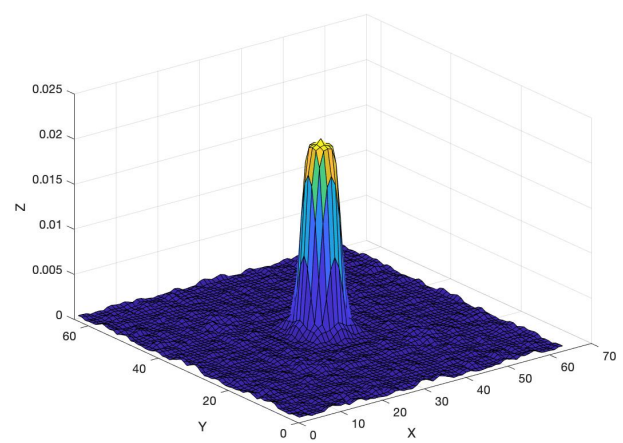
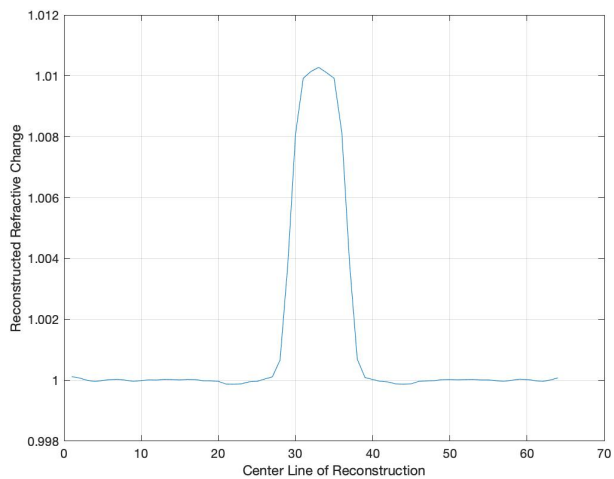


(b) Rytov Approximation

Figure 2.6: Reconstructions of a 2λ cylinder with a refractive index of 1.001.

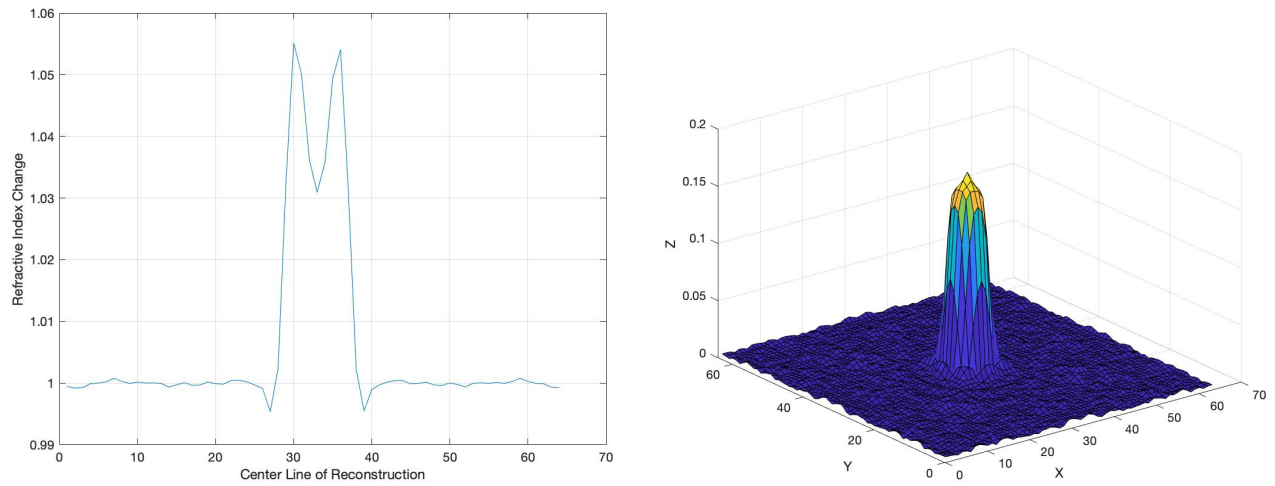


(a) Born Approximation

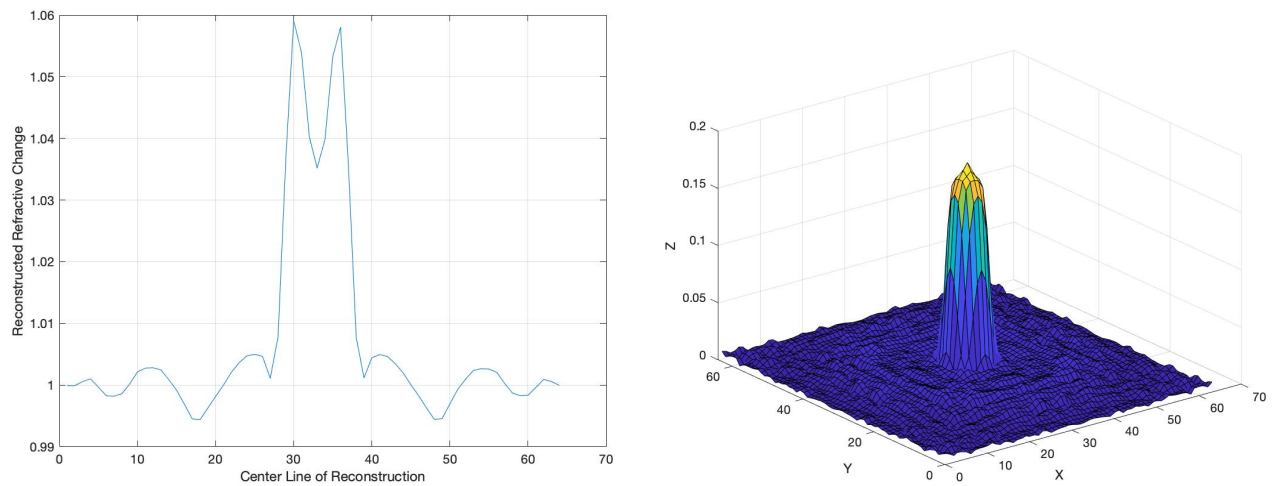


(b) Rylov Approximation

Figure 2.7: Reconstructions of a 2λ cylinder with a refractive index of 1.01.

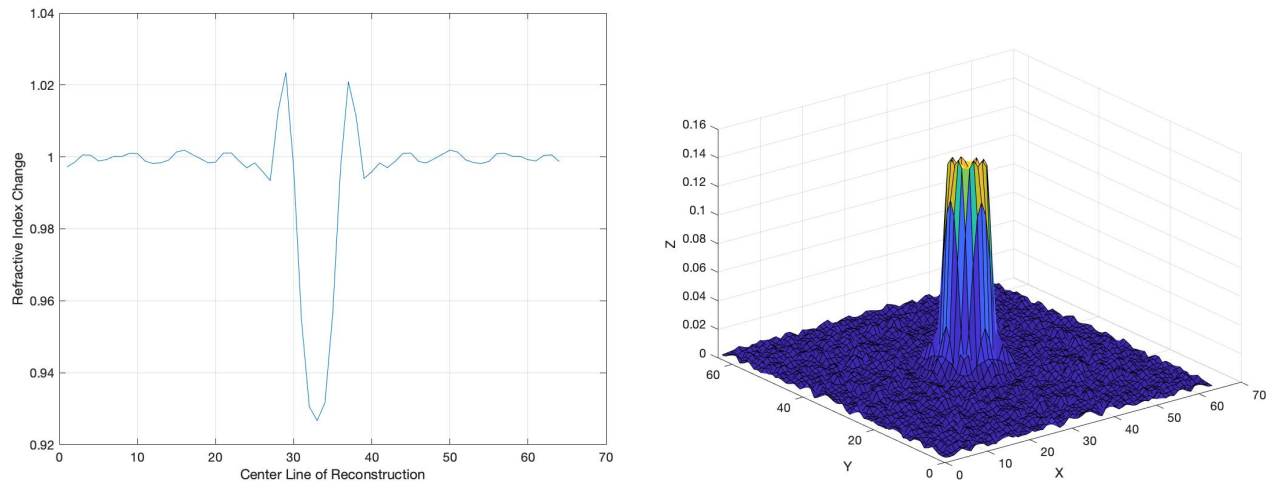


(a) Born Approximation

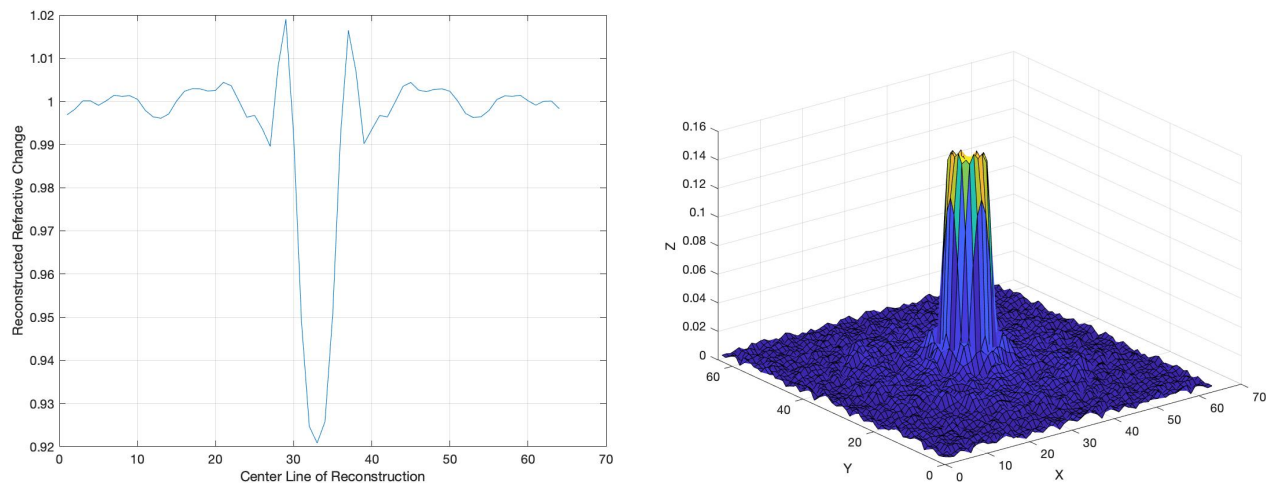


(b) Rytov Approximation

Figure 2.8: Reconstructions of a 2λ cylinder with a refractive index of 1.1.

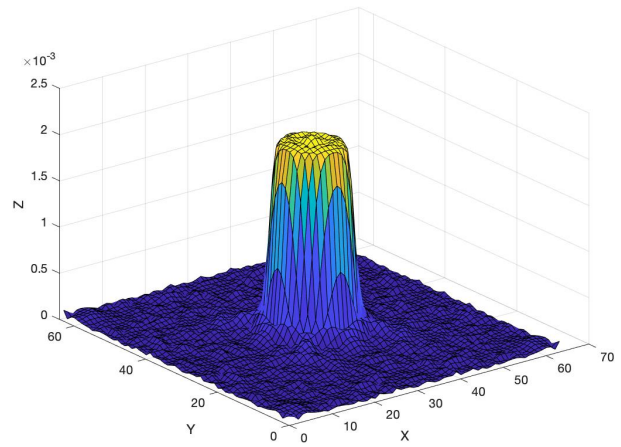
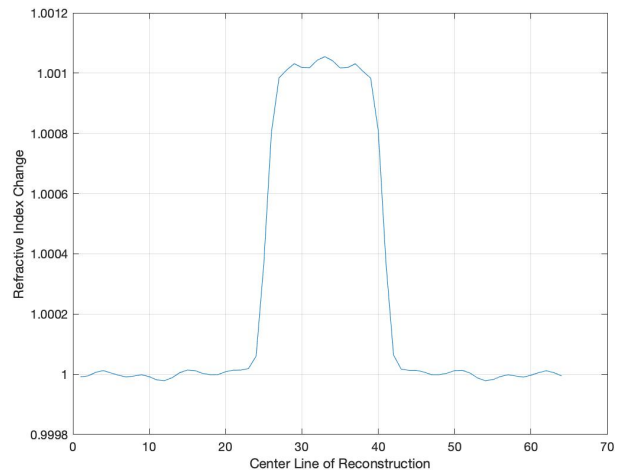


(a) Born Approximation

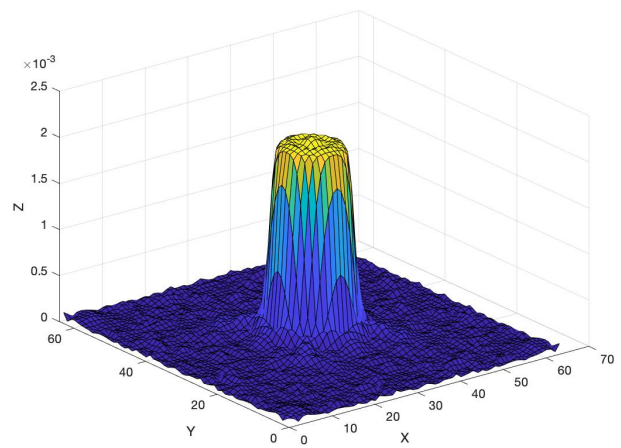
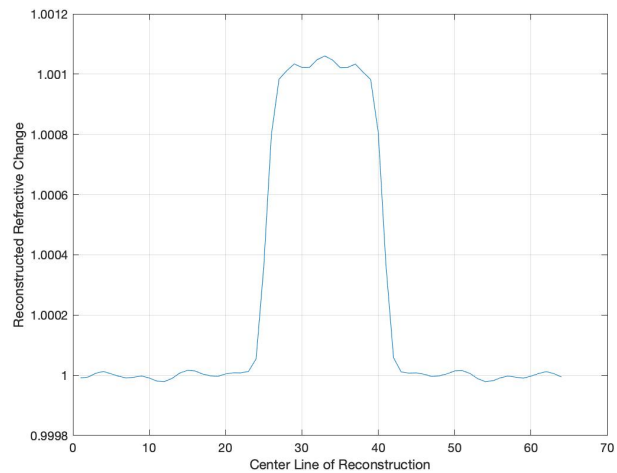


(b) Rytov Approximation

Figure 2.9: Reconstructions of a 2λ cylinder with a refractive index of 1.2.



(a) Born Approximation



(b) Rytov Approximation

Figure 2.10: Reconstructions of a 4λ cylinder with a refractive index of 1.001.

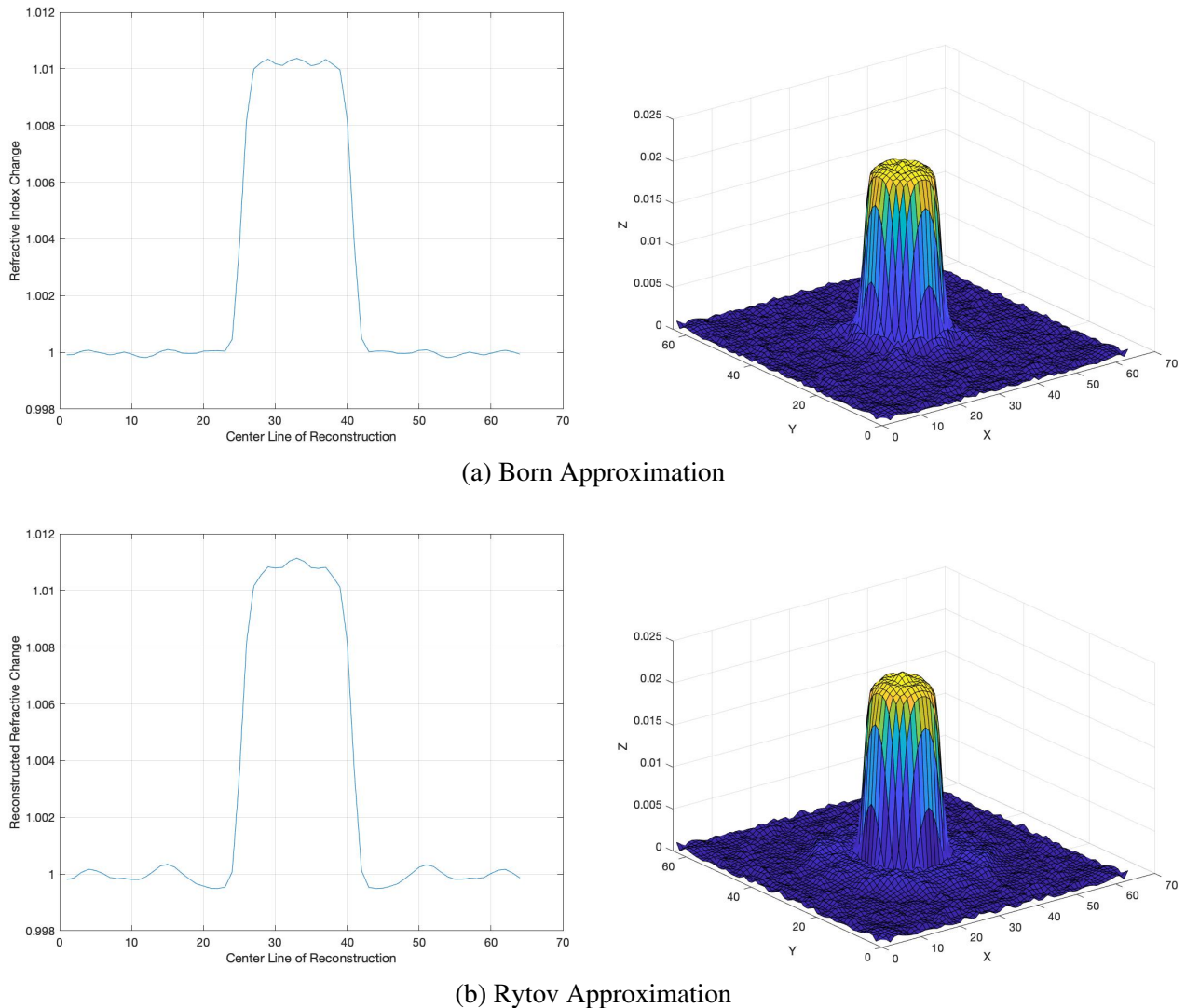
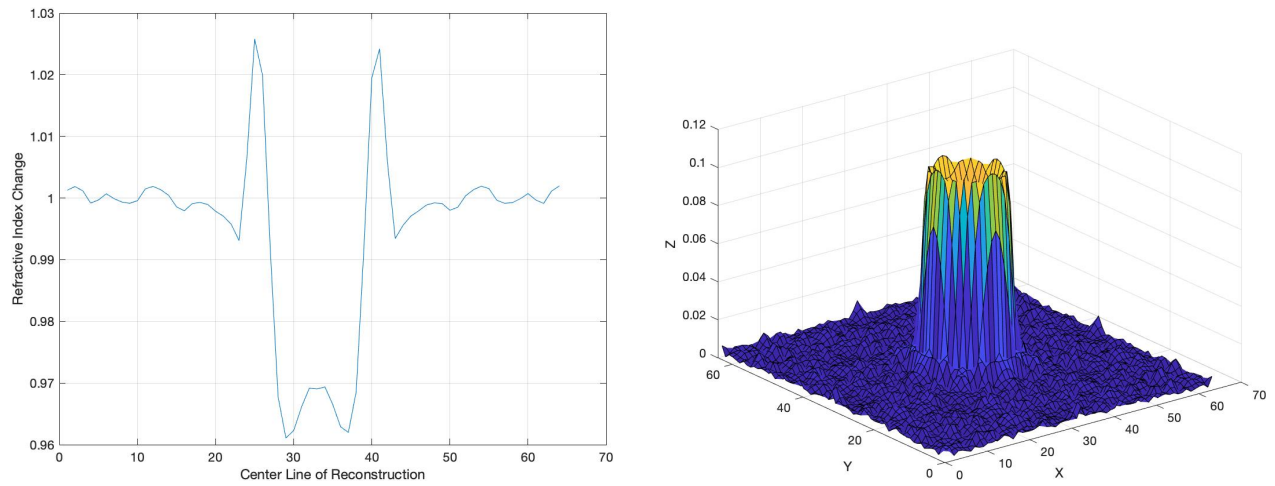
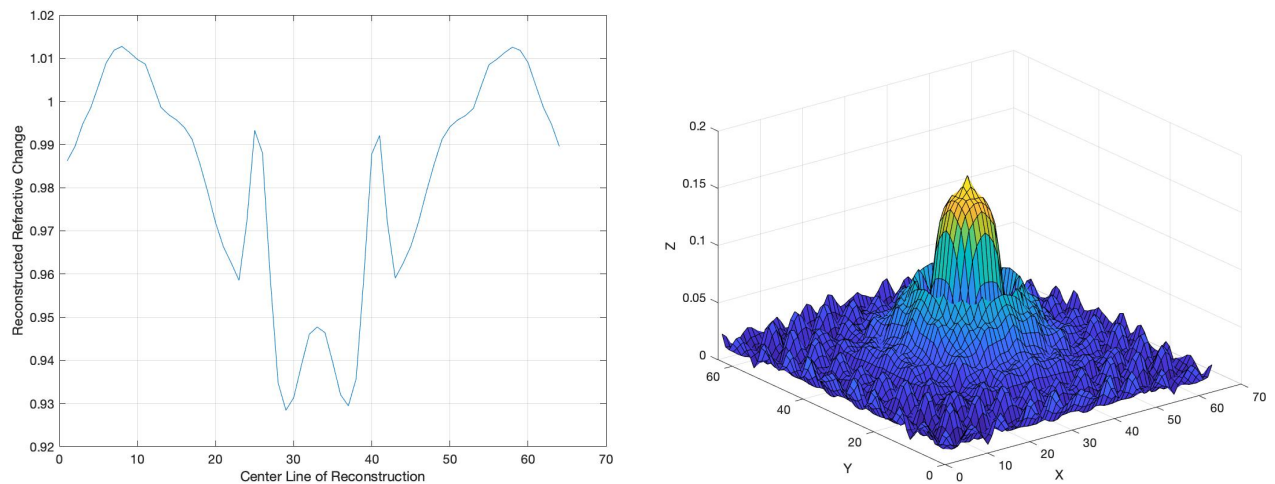


Figure 2.11: Reconstructions of a 4λ cylinder with a refractive index of 1.01.

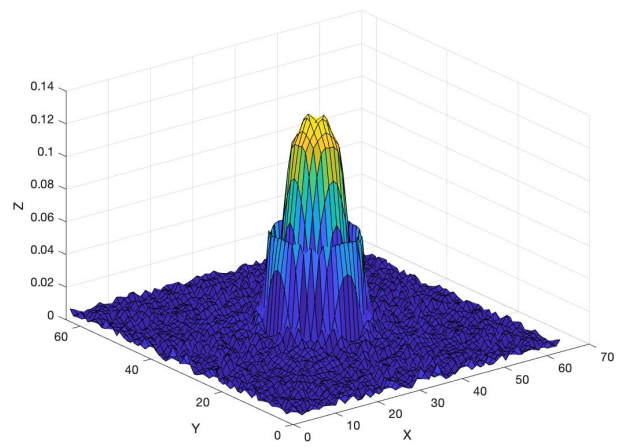
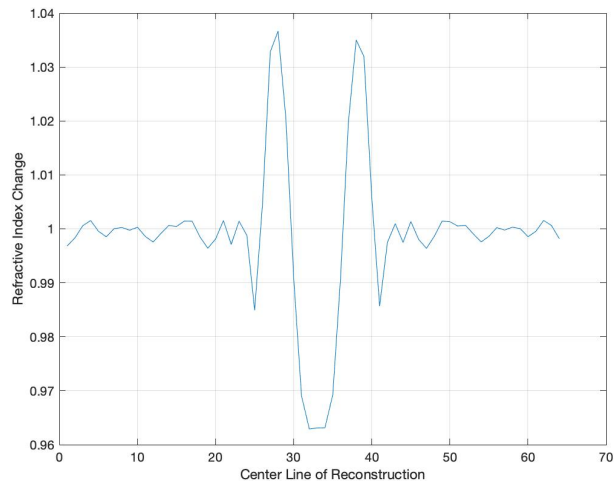


(a) Born Approximation

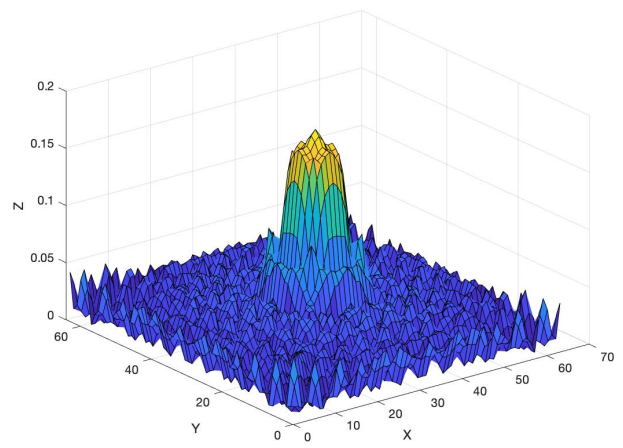
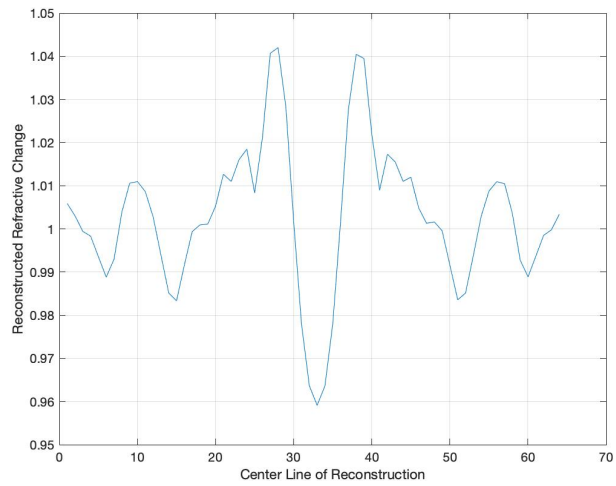


(b) Rytov Approximation

Figure 2.12: Reconstructions of a 4λ cylinder with a refractive index of 1.1.

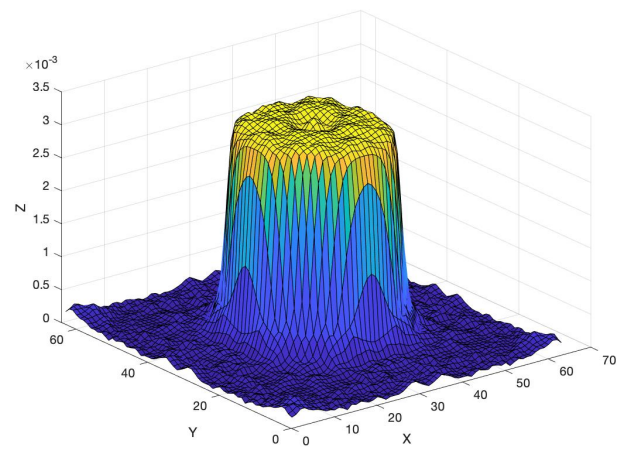
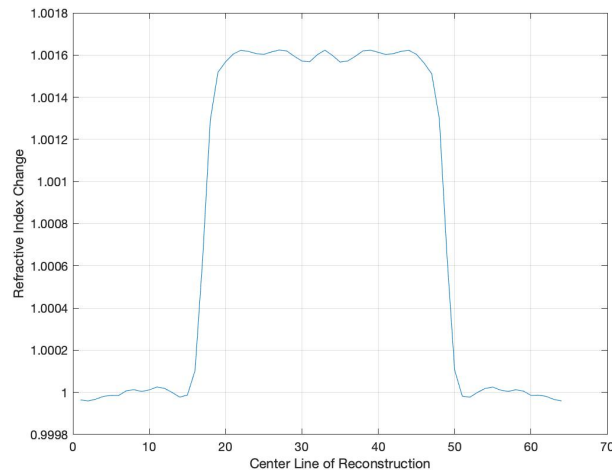


(a) Born Approximation

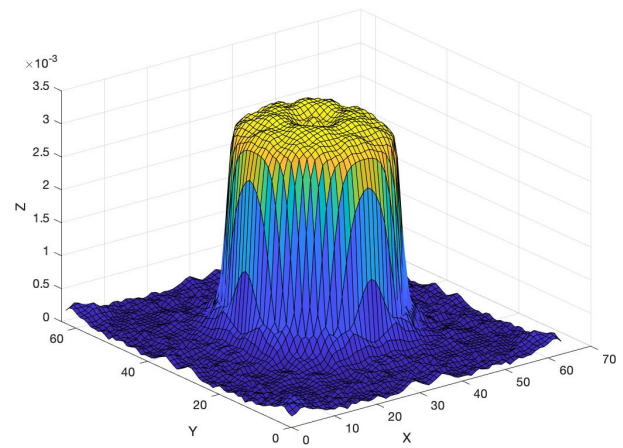
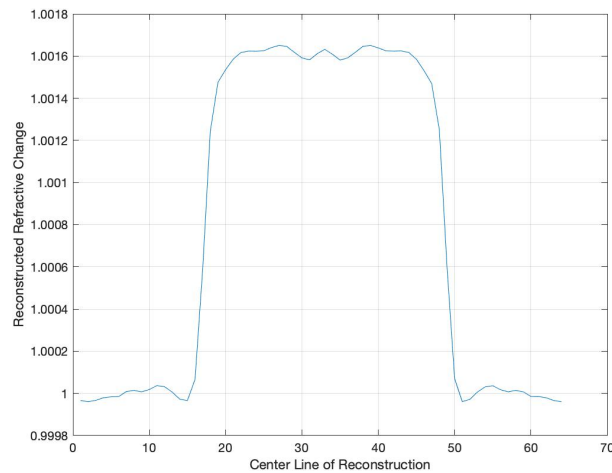


(b) Rytov Approximation

Figure 2.13: Reconstructions of a 4λ cylinder with a refractive index of 1.2.

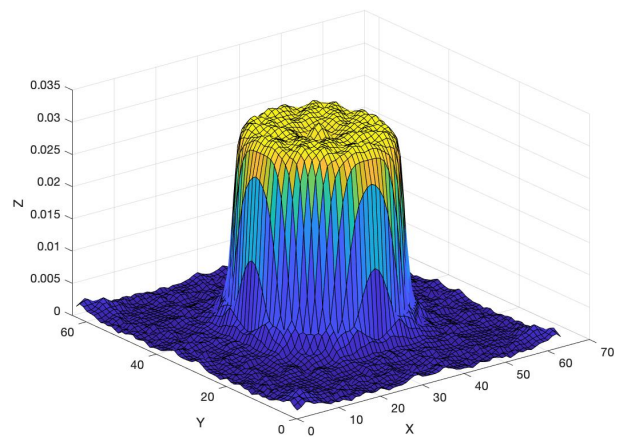
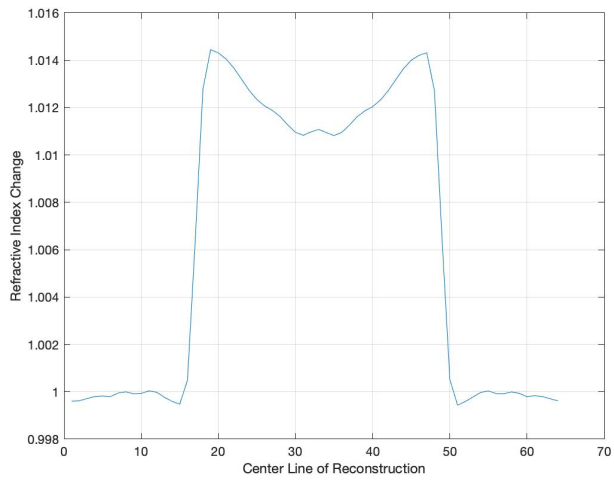


(a) Born Approximation

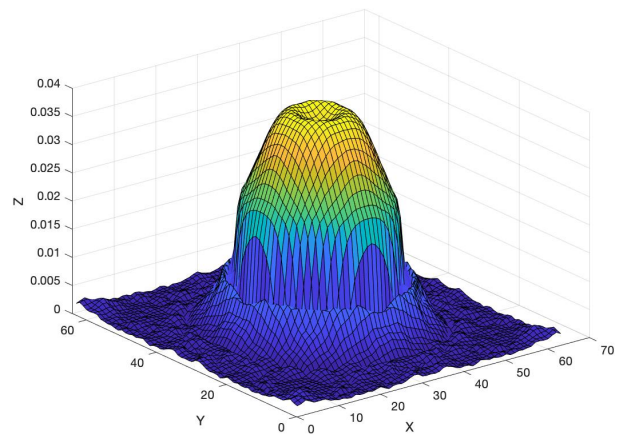
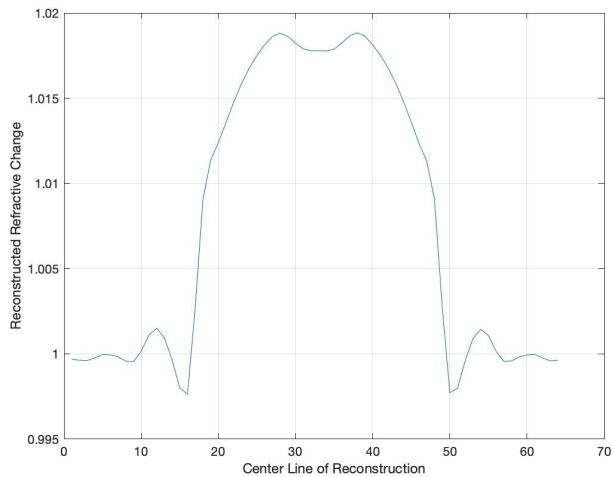


(b) Rytov Approximation

Figure 2.14: Reconstructions of a 10λ cylinder with a refractive index of 1.001.

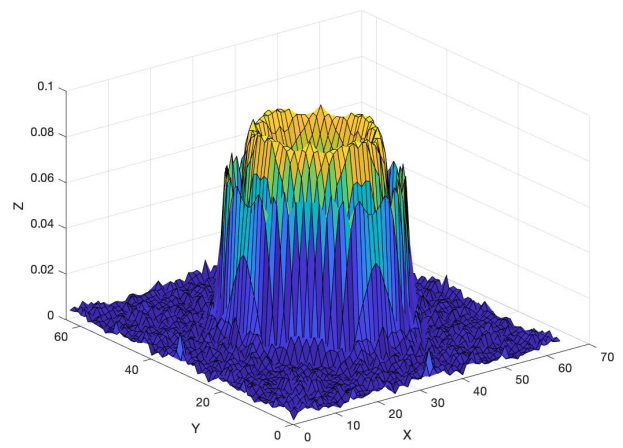
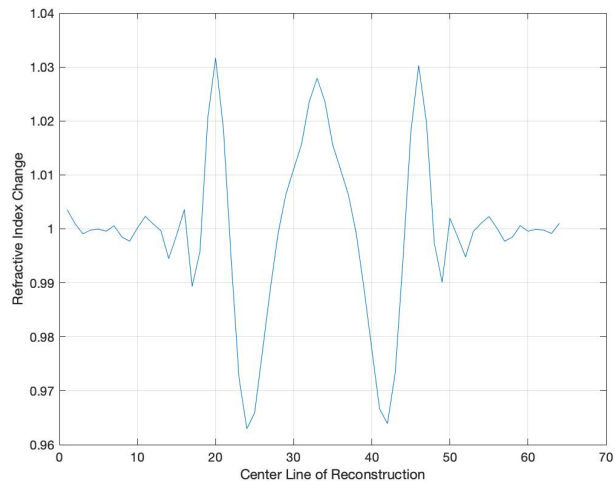


(a) Born Approximation

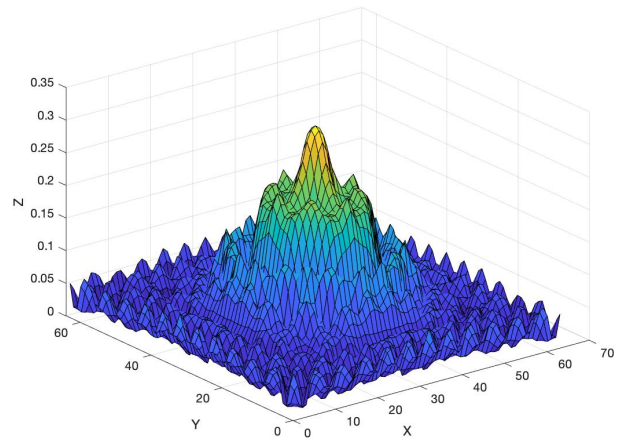
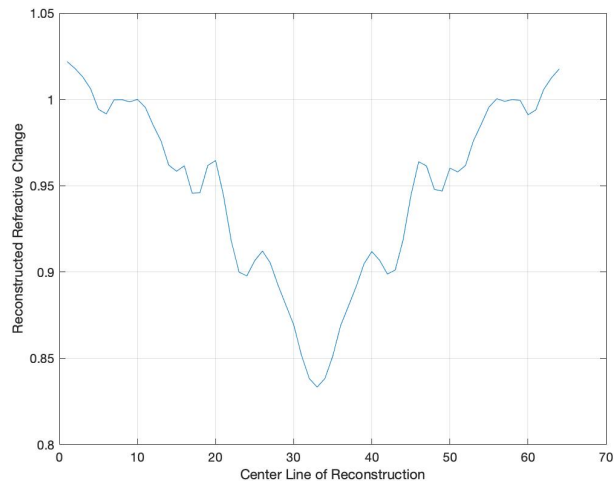


(b) Rytov Approximation

Figure 2.15: Reconstructions of a 10λ cylinder with a refractive index of 1.01.

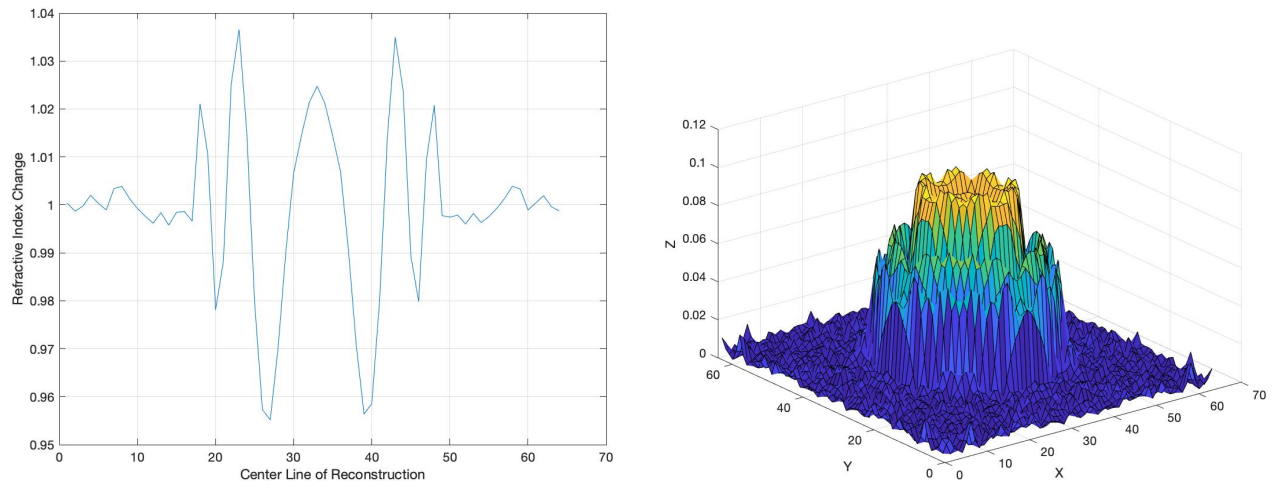


(a) Born Approximation

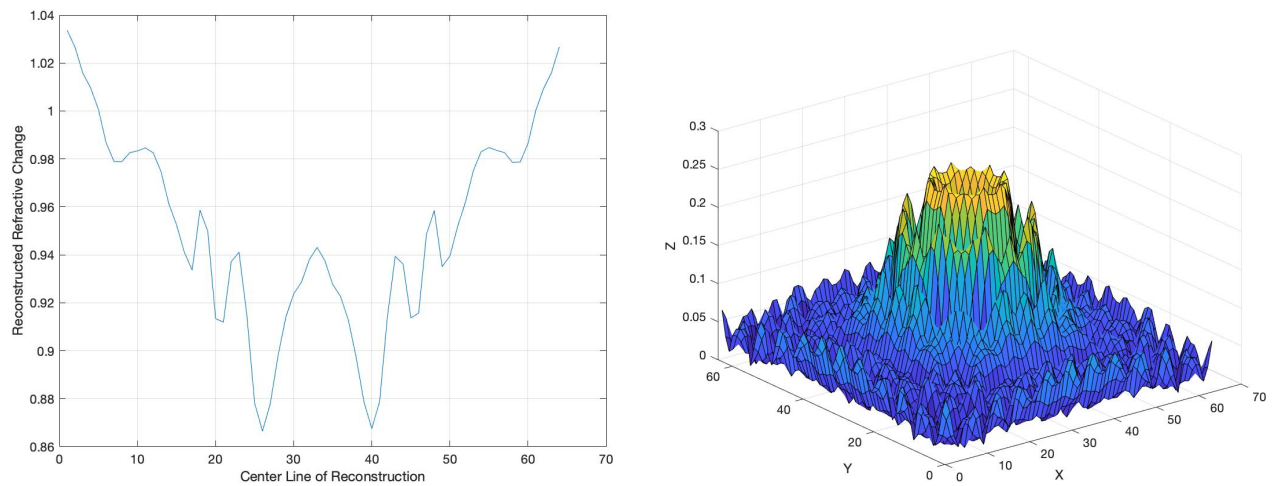


(b) Rytov Approximation

Figure 2.16: Reconstructions of a 10λ cylinder with a refractive index of 1.1.



(a) Born Approximation



(b) Rytov Approximation

Figure 2.17: Reconstructions of a 10λ cylinder with a refractive index of 1.2.

CHAPTER 3

RADIO TOMOGRAPHIC IMAGING

In this chapter, we will be focusing on the RTI approach and describing the linear model in relation to the RSSI measurements that detect the change in the attenuation which occurs when an object or human is introduced in a region with WSNs.

3.1 Model

3.1.1 Linear Formulation

In a region with WSNs, the Wi-Fi signals are transmitted and received when the Wi-Fi nodes communicated with each other. An introduction of an object or human being within the area causes absorption, diffraction, reflection or scattering of the transmitted power. The main aim of the RTI system is to determine the image vector dimension \mathbb{R}^N which will describe the amount of power attenuation that occurred due to the presence of the physical objects or human present within the N pixels of the WSNs region [7]. Fig. 3.1 displays the RTI network [7].

Given that we know the location of the pixel, RTI makes it possible to know where the attenuation of the network is happening thus making it possible to localize the position of the physical object.

Given that there are K Wi-Fi nodes deployed in the indoor room with RTI network, the total number of two-way wireless links can be denoted as $M = \frac{K^2 - K}{2}$ where reciprocity in the links is accounted for [7]. The pair of nodes are counted as a link regardless of whether a communication is actually occurring between them or not.

Now when an object is present in the room, some of the node links will be blocked by the object and this will cause the Wi-Fi signal to experience significant attenuation. The RSSI of $y_i(t)$ of a particular nodes link i at time t is dependent on the following [7]:

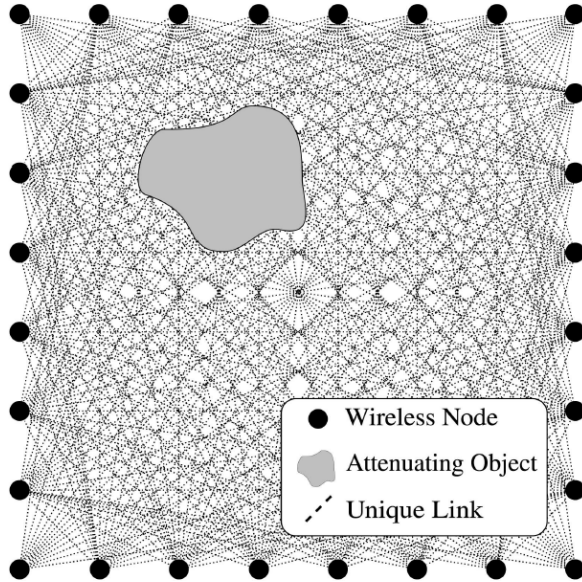


Figure 3.1: This is an illustration of the RTI network whereby each node is continuously transmitting and receiving signals to one another thus developing many projects that can be utilized to reconstruct an image of physical objects inside the WSNs.

- P_i : Transmitted power in decibel-milliwatts (dBm).
- $S_i(t)$: Shadowing loss in dBm that is caused by the presence of an object in the environment thus resulting in signal attenuation.
- $F_i(t)$: Fading loss in dBm due to destructive and constructive interference of Wi-Fi signals in the environment.
- L_i : Static losses in dBm due to distance between Wi-Fi nodes, issues in device hardware and other factors.
- $v_i(t)$: Noise measurement in the environment.

Therefore, RSSI can be denoted as:

$$y_i(t) = P_i + S_i(t) + F_i(t) + L_i + v_i(t) \quad (3.1)$$

Imaging of the region is represented by many small square regions of the same size with each small region being called a pixel. Therefore, the shadowing loss $S_i(t)$ can be approximated as the

sum of attenuation that occurs in each pixel. Let N be the total number of square pixels in the image representation of the room and x_j is the attenuation caused by the Wi-Fi signal that passes through pixel j when a link is established between two nodes at time t . Therefore, $S_i(t)$ can be denoted as:

$$S_i(t) = \sum_{j=1}^N w_{ij}x_j(t) \quad (3.2)$$

where w_{ij} is the weighting of pixel j for the established node link i . If the nodes are in line with each other and there are no pixels, the weight of the pixel will be assumed to be zero. Fig. 3.2 displays an example of how the direct LOS link is weighted in a non-scattering environment [7].

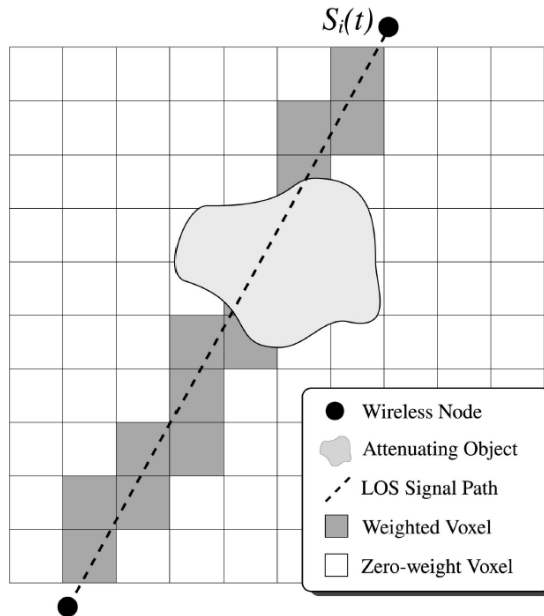


Figure 3.2: This is an illustration of a single link present in a RTI network which travels in a direct LOS path. The presence of an physical objects causes the signal to be shadowed as it crosses the area of the network in a particular path. The pixels that have been darkened represent the areas of the image where there is a nonzero weighting for that particular link.

In order to simplify the problem, imaging the change in attenuation results in the removal of the static losses over time. The change in RSSI Δy_i from time t_a to t_b which is denoted as

$$\begin{aligned} \Delta y_i &= y_i(t_b) - y_i(t_a) \\ &= S_i(t_b) - S_i(t_a) + F_i(t_b) - F_i(t_a) + v_i(t_b) - v_i(t_a) \end{aligned} \quad (3.3)$$

which can be rewritten as

$$\Delta y_i(t) = \sum_{j=1}^N w_{ij} \Delta x_j(t) + n_i \quad (3.4)$$

where n_i is the summation of the fading and measurement noise. In order to make the equation (3.4) more compact [4] with all the links in the WSNs being considered simultaneously, the RSSI expression can be simplified as:

$$\Delta \mathbf{y} = \mathbf{W} \Delta \mathbf{x} + \mathbf{n} \quad (3.5)$$

where

$$\begin{aligned} \Delta \mathbf{y} &= [\Delta y_1, \Delta y_2, \dots, \Delta y_M]^T \\ \Delta \mathbf{x} &= [\Delta x_1, \Delta x_2, \dots, \Delta x_N]^T \\ \mathbf{n} &= [n_1, n_2, \dots, n_M]^T \\ \mathbf{W} &= [w_{ij}]_{M \times N} \end{aligned} \quad (3.6)$$

and $\Delta \mathbf{y}$ represents the change in the RSSI measurements of M links, \mathbf{n} is the noise vector which will be considered negligible in the simulation results. $\Delta \mathbf{x}$ is the attenuation of the object that will be estimated. \mathbf{W} is the weights matrix with $M \times N$ dimension with the column representing the pixels and the row representing the weight of each pixel for which the particular link passes through. In order to simplify the notation, \mathbf{x} and \mathbf{y} will be used to replace $\Delta \mathbf{x}$ and $\Delta \mathbf{y}$ respectively.

3.1.2 Weight Model

In order to determine \mathbf{W} , a statistical model has been implemented that would be able to describe the linear effect of the attenuation field on the path loss for each link [7]. The ellipse model was proposed by [7] as a means of weighting pixels. For a particular link, the two nodes will be the foci of an ellipse and if a pixel falls inside the ellipse, the weight of the corresponding pixel will be set to 1, otherwise it will be zero. The weight will be normalized to $\frac{1}{\sqrt{d}}$ since the distance between two nodes of the link are different. The weighting can be defined as

$$\mathbf{w}_{ij} = \frac{1}{\sqrt{d}} \begin{cases} 1 & \text{if } d_1 + d_2 < d + \delta \\ 0 & \text{otherwise} \end{cases} \quad (3.7)$$

where d is the distance between two nodes, d_1 and d_2 are distances from pixel j and the two nodes respectively for link i . δ is the adjustable parameter which is the width of the ellipse which in a typical RTI model should be set low such that it is identical to using the LOS weighting model [4]. In order to ensure that we are using the LOS model as depicted in Fig. 3.2, we have decided to set the width parameter of δ to be low in RTI. This ellipsoid methodology has been used as a simplification process in determining which pixels are present along the LOS path.

3.2 Image Reconstruction

3.2.1 Simulation Setup

For the simulation setup, we have decided to consider a square perimeter which has been fitted with 20 Wi-Fi sensor nodes in order to collect the RSSI measurements as shown in Fig 3.3. Our imaging problem can then be defined as detecting and localizing changes in the environment within the perimeter.

To perform full electromagnetic simulation of our target room ($3\text{ m} \times 3\text{ m} \times 4\text{ m}$ (room height)) corresponds to an approximate electrical volume of 18500 cubic wavelengths (approximately 24 by 24 by 32 wavelength). In general this would require significant computing resources if full 3D electromagnetic simulation was to be performed computing RF signals.

To overcome the problem of the large computation size of the problem, we therefore made a number of simplifying assumptions. The first is the assumption that only vertical polarization is considered. This has been performed previously [8] and is based on the radio being vertically polarized and that cross-polarization scattering is assumed not to be significant. The second assumption is that we approximate the room by a 2D rectangle with the same cross-section as the plan shown in Fig. 3.3. This assumption is severe but will also be valid if the antennas used at the Wi-Fi nodes are sufficiently directive so as to avoid significant LOS reflections from the ceiling and floor. Finally, we simplify the object of interest in the room by using a dielectric cylinder at any location with a particular radii and varying permittivities. This assumption is justified on the bases of detecting change with a focus on detecting a movement of humans or furniture in the room. Although a human body does not have an exact circular shape we approximate as such with permittivity ranging

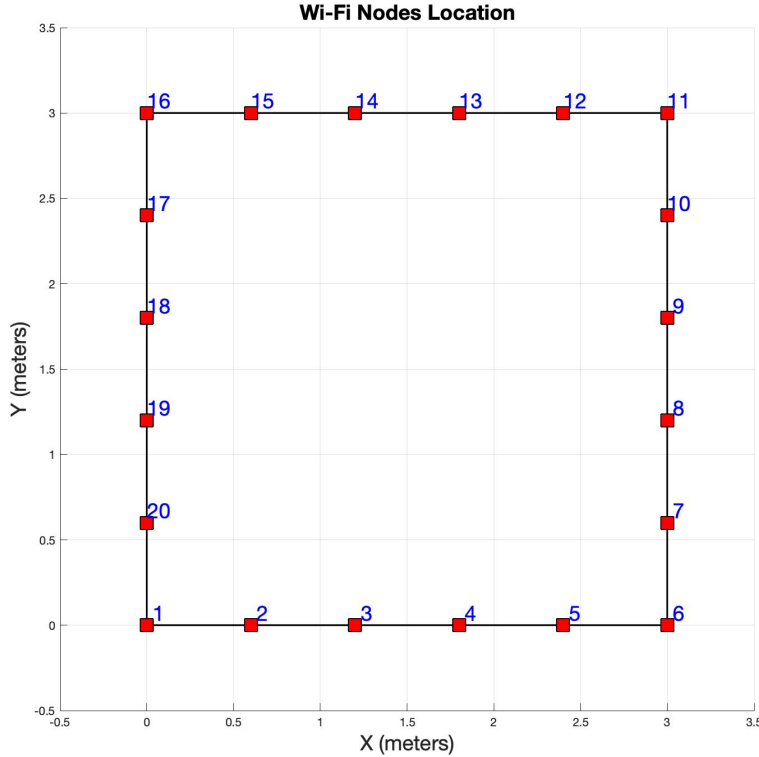


Figure 3.3: Arrangement of the Wi-Fi sensor nodes in a two-dimensional cross-section of a room with dimensions of 3 m by 3 m.

from 20 to 60 [20]. Objects like furniture in room are taken to have permittivity ranging from 2 to 6 [21] at the frequency of 2.4 GHz.

With these assumptions in place, we can calculate the electromagnetic field exactly by using traditional eigenfunction expansions and mode matching. We express the coordinates of the problem in circular coordinates and utilize Bessel functions expansions of the transmitter and scattered field following the approach described in standard electromagnetic books [22]. Using this approach and assumptions, we can find the exact electromagnetic field and subsequently the RSSI, at any point within the room caused by the presence of a circular dielectric cylinder due to a transmitting source at any location.

The focus is to detect the change in the environment and this change is simulated by the presence or absence of a cylinder with varying permittivities. We simulate a cylinder with a radii 0.3 m with the center at (2, 2) as shown in Fig. 3.4.

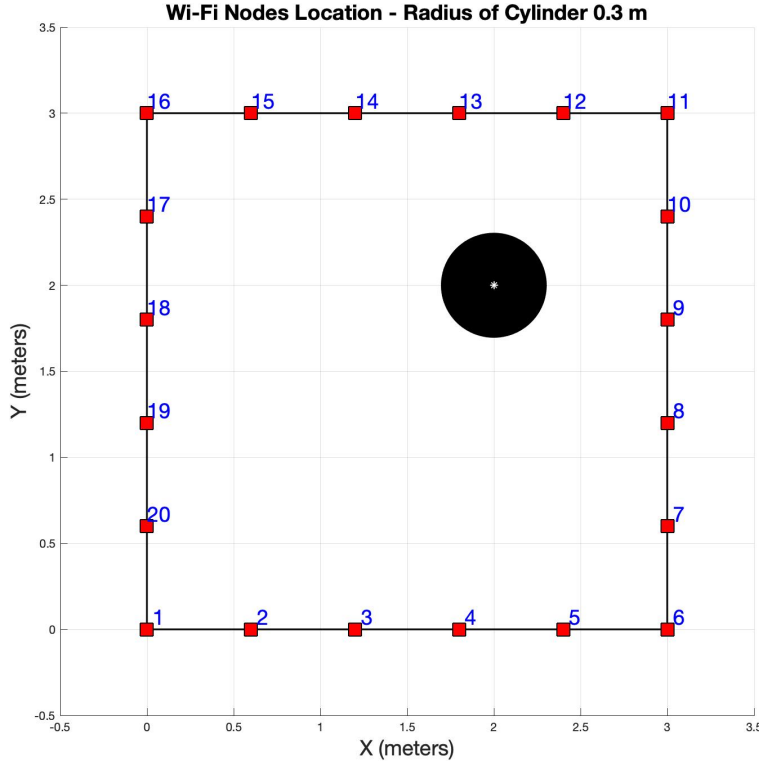


Figure 3.4: Cylinder with a radius of 0.3 m with the center positioned at (2, 2) and the permittivities being arbitrary.

The three permittivities that we simulate are 1.5, 3 and 30. The radii of 0.3 m with permittivities of 1.5 and 3 is a representation of objects such as furniture i.e. wooden table, chair etc. Meanwhile, the radii of 0.3 m with permittivity of 30 is a representation of a human walking in a room.

3.2.2 Ill-Posed Inverse Problem and Simulation Results

The linear model of RTI can be denoted in a simplified manner as denoted in equation 3.8

$$\mathbf{y} = \mathbf{W}\mathbf{x} + \mathbf{n} \quad (3.8)$$

whereby $\mathbf{y} \in \mathbb{R}^M$ represented the measured data, $\mathbf{W} \in \mathbb{R}^{M \times N}$ is the transfer weighting matrix of the model parameters $\mathbf{x} \in \mathbb{R}^N$ with $\mathbf{n} \in \mathbb{R}^M$ is a noise vector which can be considered negligible. In order to estimate an image from the measurement data, an optimal solution approach is least-

squared-error as discussed in [7] where

$$\mathbf{x}_{LS} = \arg \min_{\mathbf{x}} \|\mathbf{W}\mathbf{x} - \mathbf{y}\|_2^2 \quad (3.9)$$

Equation (3.9) minimizes the noise energy in order to fit the measured data to the model. By setting the gradient of equation (3.9) equal to zero, it results in

$$\mathbf{x}_{LS} = (\mathbf{W}^T \mathbf{W})^{-1} \mathbf{W}^T \mathbf{y} \quad (3.10)$$

which is only valid if \mathbf{W} is full rank matrix but it is not valid in the case of the RTI system [7]. Using the least-squared-error approach, let us first examine the reconstruction of the 0.3 m cylinder with the three different permittivities and pixel size of 1 as shown in Figs. 3.5-3.7.

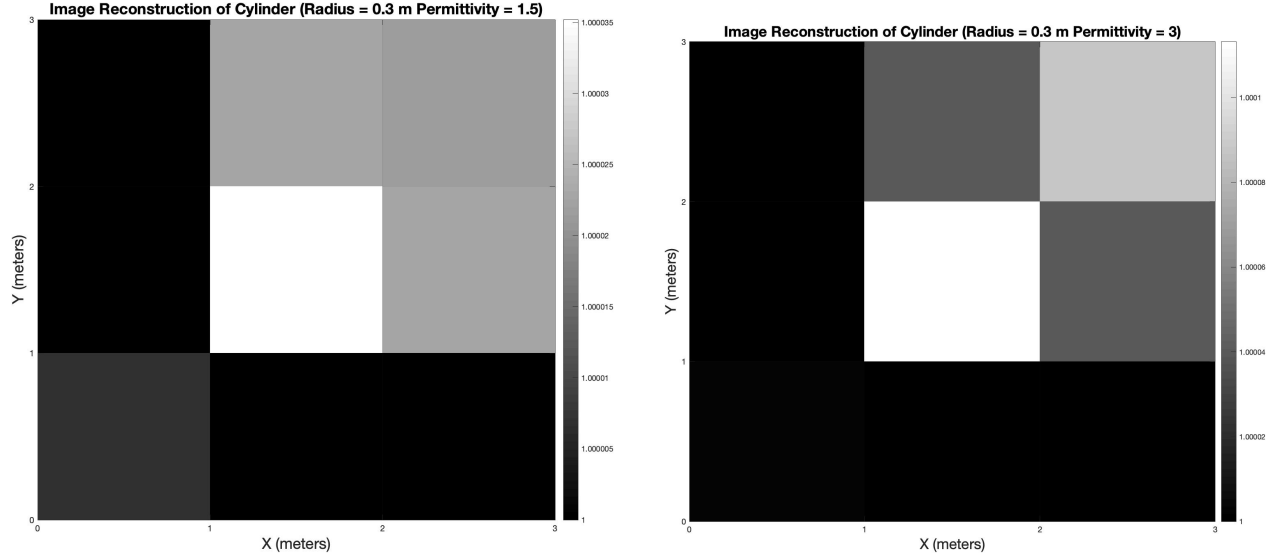


Figure 3.5: RTI reconstruction of cylinder using the least-squared-error approach with radius of 0.3 m, permittivity of 1.5 and pixel size of 1.

Figure 3.6: RTI reconstruction of cylinder using the least-squared-error approach with radius of 0.3 m, permittivity of 3 and pixel size of 1.

Based on the results from Figs. 3.5-3.7, we can see that the position of the reconstruction is correct however, such a reconstruction provides a poor indication on the size of the cylinder. Hence, Figs. 3.8-3.10 display the results of reconstruction of the 0.3 m cylinder with the three different permittivities and pixel size of 0.5.

Figs. 3.8-3.10 do provide better results when the reconstruction of the cylinder is done at a pixel size of 0.5. However, it is still quite difficult to recognise the size of the object that is being

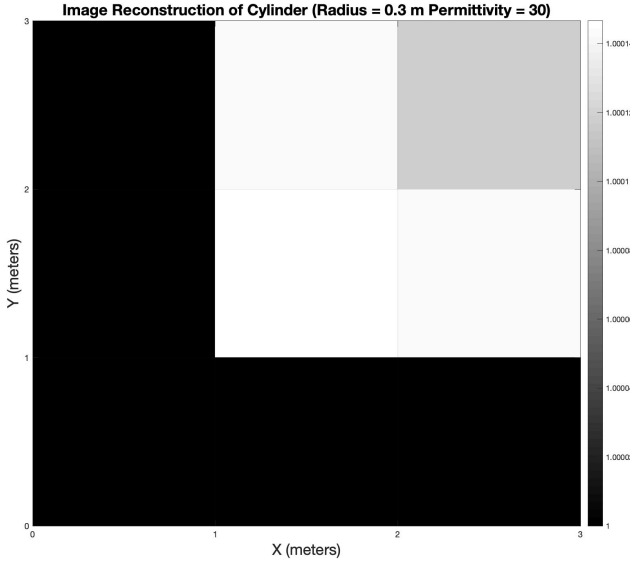


Figure 3.7: RTI reconstruction of cylinder using the least-squared-error approach with radius of 0.3 m, permittivity of 30 and pixel size of 1.

reconstructed. In our simulated configuration, we have only deployed $K = 20$ Wi-Fi nodes thus giving us only $M = 190$ unique measurements and therefore low resolution. With such a small measurement set of $M = 190$, the maximum resolution we can achieve is around 0.21 m by 0.21 m ($N \approx 190$). Figs. 3.11-3.13 show the reconstructions of the 0.3 m cylinder with the three different permittivities and pixel size of 0.5 by using the least-squared-error approach.

Figs. 3.11-3.13 are definitely providing us with better reconstruction results and as we examine Fig. 3.11, we can see that the reconstruction of the cylinder at low permittivity of 1.5 is also failing.

However, given that our aim is to detect change in the environment at a high resolution, we decided to choose pixel size of 0.1 m by 0.1 m ($N = 900$) which is the typical wavelength of Wi-Fi signals at frequency 2.4 GHz. Therefore, this becomes an example of a highly underdetermined problem ($N = 900, M = 190, N \gg M$) whereby the number of unknowns is larger than the number of measurements [14]. As a result, imaging is performed with only 21% of measurements. Given that the imaging change is performed in successive frames, we can make the assumption that spatial verification in the region of interest will be sparse. Hence, we can implement the total variation-based regularization as proposed in [23]. Therefore, the final optimization problem

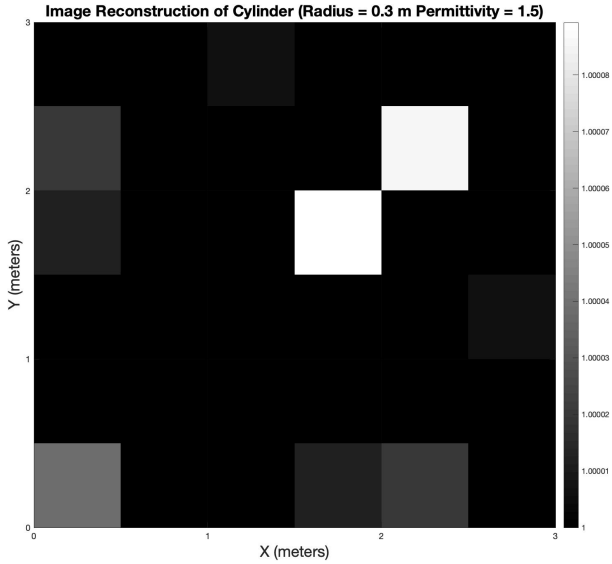


Figure 3.8: RTI reconstruction of cylinder using the least-squared-error approach with radius of 0.3 m, permittivity of 1.5 and pixel size of 0.5.

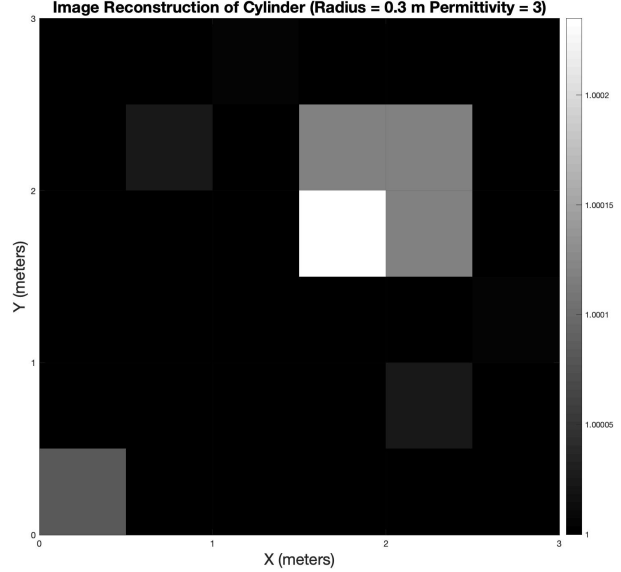


Figure 3.9: RTI reconstruction of cylinder using the least-squared-error approach with radius of 0.3 m, permittivity of 3 and pixel size of 0.5.

becomes as expressed in equation (3.11).

$$\mathbf{x}_{TVAL} = \arg \min_{\mathbf{x}} \|\mathbf{y} - \mathbf{Wx}\|_2^2 + \alpha \|\mathbf{Dx}\|_1 \quad (3.11)$$

where α is the regularization parameter and operator \mathbf{D} is the difference between successive elements of vector \mathbf{x} . Figs. 3.14-3.16 display the reconstruction of the 0.3 m cylinder with the three different permittivities and pixel size of 0.1 by using the total variation-based regularization approach.

Similarly, if we decided to choose pixel size of 0.05 m by 0.05 m ($N = 3600$) and with $M = 190$ measurements, total variation-based regularization is performed with about 5.3% of measurements in order to perform imaging. Figs. 3.17-3.19 display reconstruction at the pixel size of 0.05.

Based on Figs. 3.15, 3.16, 3.18 and 3.19 it can be seen that the RTI methodology with the implementation of total variation-based regularization is able to reconstruct the cylinders with the permittivities of 3 and 30 respectively reasonably well. Furthermore, these cylinders also have a proper localization as it is visible that the center of the reconstructed cylinders is at (2, 2). However,

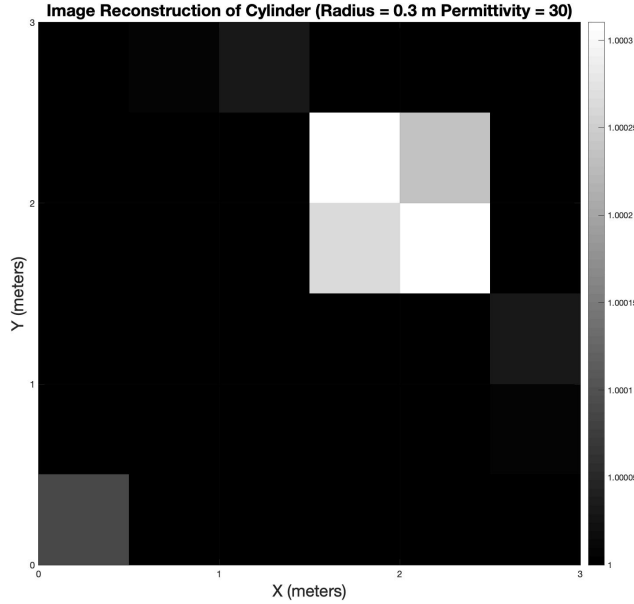


Figure 3.10: RTI reconstruction of cylinder using the least-squared-error approach with radius of 0.3 m, permittivity of 30 and pixel size of 0.5.

upon looking at Figs. 3.14 and 3.17, the RTI methodology is unable to reconstruct the cylinder with a low permittivity of 1.5 and hence, it is difficult to localize the cylinder.

Since the LOS weighting model is directly dependent on the shadowing effect of the cylinder, the cylinder with a low permittivity will result in the object having a significantly smaller shadowing effect. Furthermore, the LOS approach does not include the impact of the scattered field into the weighting model as compared to other inverse scattering techniques [14]. As a result, the small shadowing effect and neglect of scattering results in the RTI failing to reconstruct the cylinder with low permittivity thus failing to localize the object. Our empirical study also showed that RTI fails approximately below the permittivity of 3.

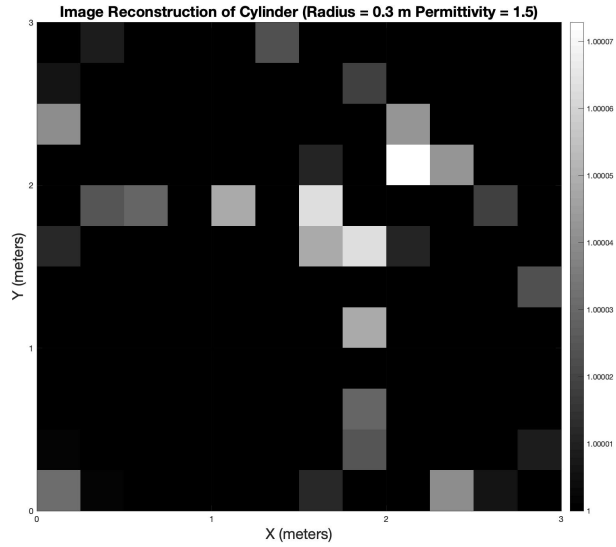


Figure 3.11: RTI reconstruction of cylinder using the least-squared-error approach with radius of 0.3 m, permittivity of 1.5 and pixel size of 0.25.

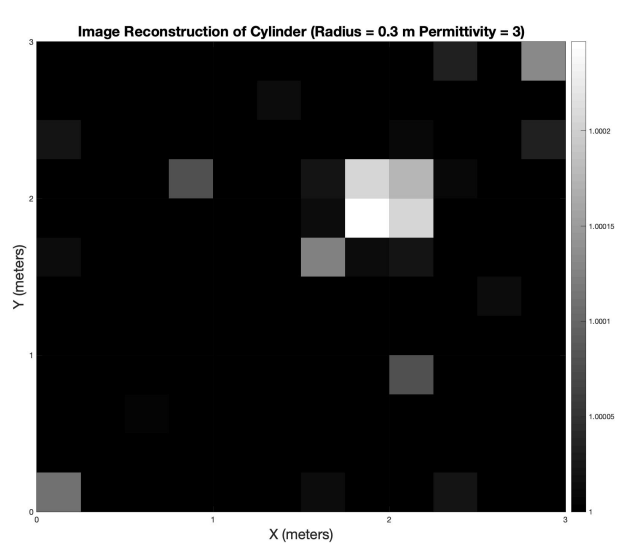


Figure 3.12: RTI reconstruction of cylinder using the least-squared-error approach with radius of 0.3 m, permittivity of 3 and pixel size of 0.25.

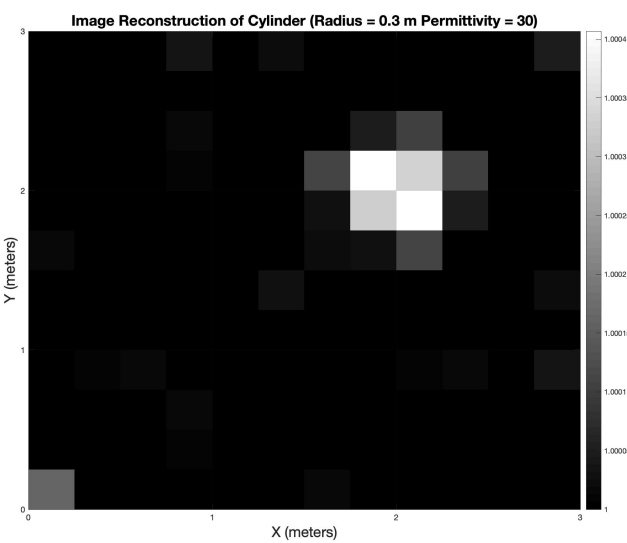


Figure 3.13: RTI reconstruction of cylinder using the least-squared-error approach with radius of 0.3 m, permittivity of 30 and pixel size of 0.25.

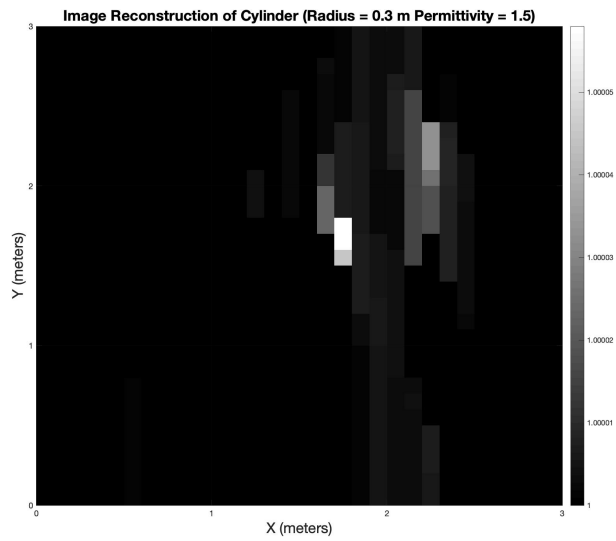


Figure 3.14: RTI reconstruction of cylinder using the total variation-based regularization approach with radius of 0.3 m, permittivity of 1.5 and pixel size of 0.1.

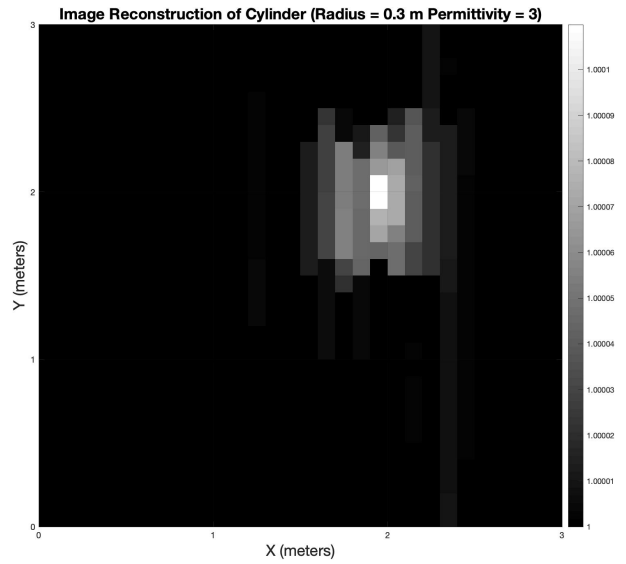


Figure 3.15: RTI reconstruction of cylinder using the total variation-based regularization approach with radius of 0.3 m, permittivity of 3 and pixel size of 0.1.

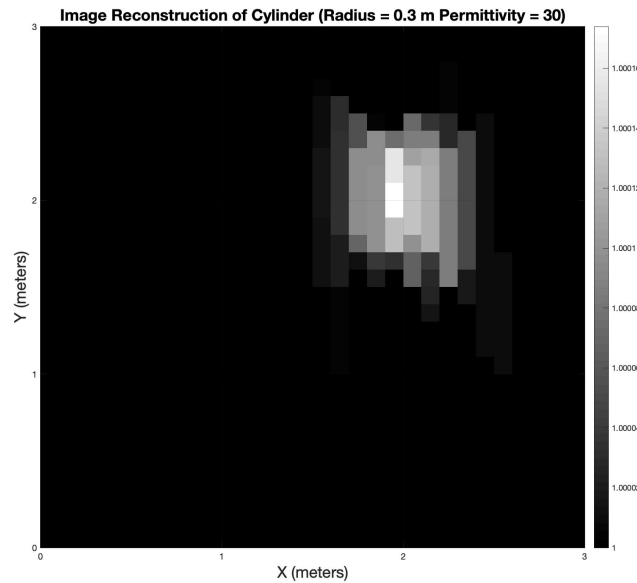


Figure 3.16: RTI reconstruction of cylinder using the total variation-based regularization approach with radius of 0.3 m, permittivity of 30 and pixel size of 0.1.

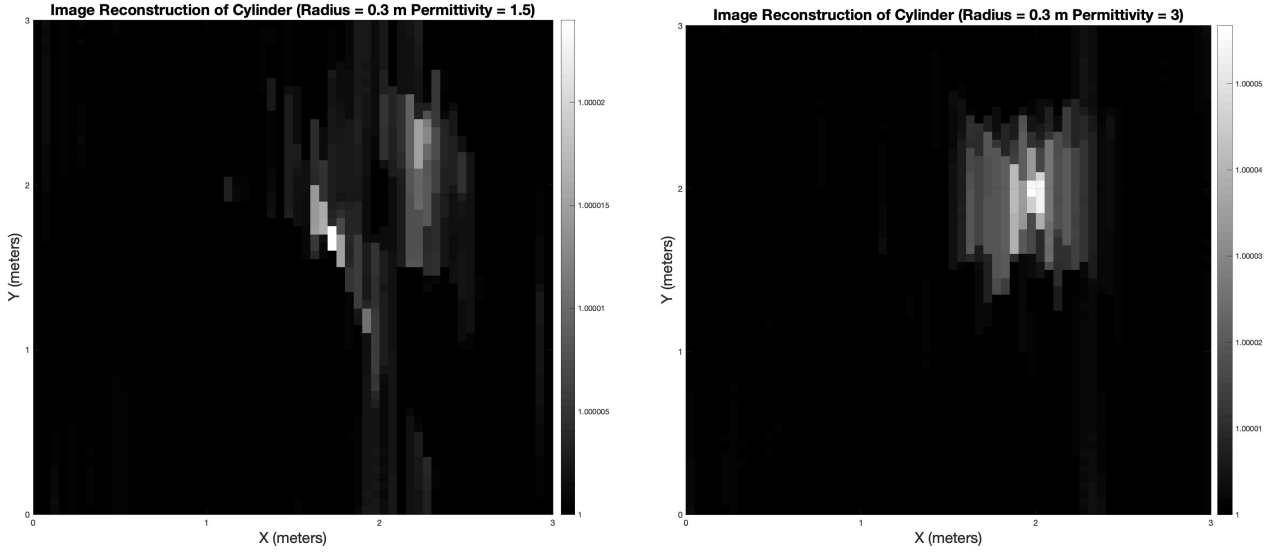


Figure 3.17: RTI reconstruction of cylinder using the total variation-based regularization approach with radius of 0.3 m, permittivity of 1.5 and pixel size of 0.05.

Figure 3.18: RTI reconstruction of cylinder using the total variation-based regularization approach with radius of 0.3 m, permittivity of 3 and pixel size of 0.05.

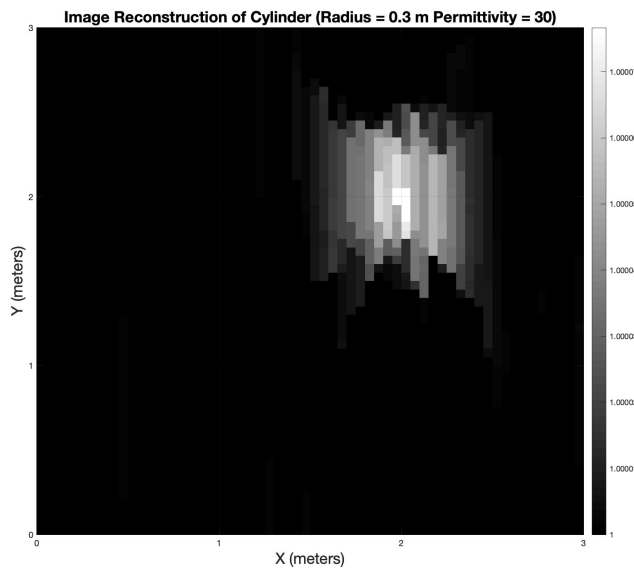


Figure 3.19: RTI reconstruction of cylinder using the total variation-based regularization approach with radius of 0.3 m, permittivity of 30 and pixel size of 0.05.

CHAPTER 4

EXPERIMENTAL SETUP AND RESULTS

After developing and understanding the fundamentals of RTI and obtaining results on the basis of simulations, the next plan was to conduct and perform experiments. In this chapter, we will be focusing on the experiment design by describing the hardware modules implemented, the programming code designed to collect and process the data and the results that have been obtained by implementing the methodology as discussed in Chapter 3.

4.1 Multiple Wi-Fi Node Measurement System

4.1.1 Design of the System

The aim of the multiple Wi-Fi node measurement system is to record the RSSI levels between the multiple Wi-Fi nodes that are continuously transmitting and receiving Wi-Fi signals. In order to establish the WSN, we have decided to configure each of the Wi-Fi module as an Access Point (AP), thus making it a suitable portal for devices to connect to a local area network. In addition, it has also been configured as a Station (STA) whereby it can act as a wireless client and connect to other APs or Routers [24].

All the other Wi-Fi nodes in the WSN utilize the AP beacon signal in order to determine the RSSI levels of the beacon. Subsequently, the STA present at the node makes it possible to scan the Wi-Fi channels in order to obtain the RSSI levels from all the other nodes present in the WSN by using their AP beacons. Afterwards, the data from each of Wi-Fi node module is sent to the server through a Wi-Fi router and stored as a file. Suppose we have N nodes, then we will be having $N^2 - N$ unique RSSI measurements for every scan cycle that occurs with both the channel and its reciprocal channel being measured independently [24].

4.1.2 Hardware Details

The hardware modules utilized for the Wi-Fi nodes are the SparkFun ESP32 Thing boards which are connected to a Wi-Fi AP. The reason that we have decided to use these boards is because of its power and versatility that makes it a strong foundation for many Internet of Things (IoT) related projects. In addition, there are quite inexpensive and not very complex to configure and program [24]. The hardware details of the SparkFun ESP32 Thing board are present in [25].

Each of the ESP32 Wi-Fi node has been configured as a soft AP with a SSID, "MeasureXX" whereby the "XX" represents a specific board number of the ESP32. All the AP's contain "Measure" in their SSID with their corresponding RSSI value that is sent via UDP [24], which is then sent through the Wi-Fi router and then to a server. As a result, the server processes the data and then stores the SSID and its corresponding RSSI values in a log file.

In order to improve the imaging results, we have decided to incorporate directional antennas. In order to hold the directional antenna, we have soldered an electromechanical fixture onto the ESP32 board as shown in Fig. 4.1.

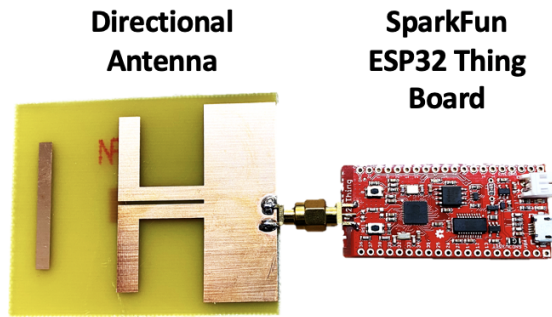


Figure 4.1: Electromechanical fixture between SparkFun ESP32 Thing Board and Directional Antenna.

4.1.3 Details about the Directional Antenna

We have decided to use a FR4 Epoxy Board to design the directional antennas as these boards are quite inexpensive and have high fabrication tolerances. Fig. 4.2 displays the measurement gain of

the directional antenna. Given that we are using Wi-Fi signals for our experimentation that has

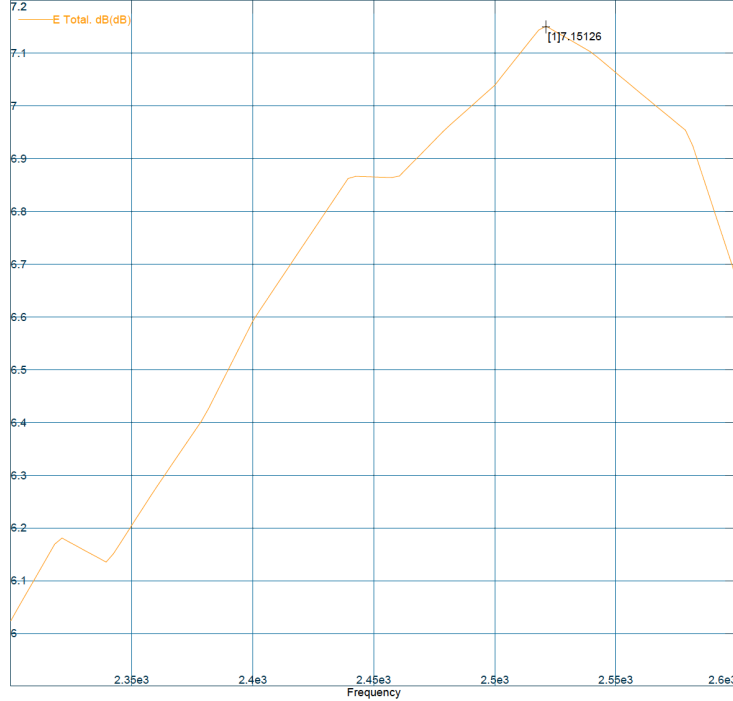


Figure 4.2: Measurement gain of the directional antenna at different frequencies.

a frequency of 2.4 GHz, the directional antenna has a gain of 6.6 dBi thus making it suitable for our experiments. Fig. 4.3 displays the radiation pattern of the directional antenna at different plane positions.

For our experimentation, the antenna was positioned at $\phi = 0$ plane as this minimized the impact of ground reflections. In addition, by positioning the antenna at $\phi = 0$ plane, the radiation pattern in Fig. 4.3 shows that there is minimal gain at the backside of the directional antenna thus minimizing the reflections from the wall in the indoor environment. Such radiation pattern and high gain of the directional antenna ensures that there is a reduction in scattering which results in better performance for the linearized RTI model.

When a signal from a transmitter is applied to an antenna, electromagnetic waves are sent out in free-space. Hence, the electromagnetic field characteristics tend to vary as a function of distance from the antenna which can be classified as near-field region and far-field region [26]. The near-field region is the region that is defined right next to the antenna. This can be further divided into

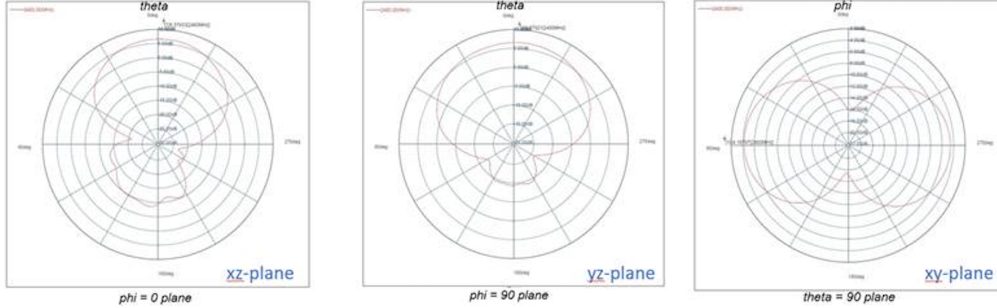


Figure 4.3: Radiation pattern of directional antenna at different plane positions of $\phi = 0$, $\phi = 90$ and $\theta = 0$.

regions which are reactive near field and radiative near field. The reactive near field is the region that is adjacent to the directional antenna. In this region, the E-field and H-field are 90 degrees out of phase with regards to each other and are reactive. In order to propagate, the E/H fields need to be orthogonal and in phase with each other [26]. It is denoted in equation (4.1)

$$Reactive\ Near\ Field\ Region \leq 0.62\sqrt{\frac{D^3}{\lambda}} \quad (4.1)$$

where D is the maximum linear dimension of the antenna and λ is the wavelength the radiating wave. Since the frequency of the Wi-Fi signal is 2.4 GHz and the maximum linear dimension of the antenna is 7.5 cm (0.075 m), the reactive near field region of the directional antenna is less than or equal to 3.6 cm (0.036 m).

Radiative near field is the region between reactive near field and far field whereby the electromagnetic fields start to transition from reactive to radiating field but not having completely transitioned as the shape of the radiation still varies with distance [26]. It is denoted in equation (4.2)

$$0.62\sqrt{\frac{D^3}{\lambda}} \leq Radiative\ Near\ Field\ Region \leq \frac{2D^2}{\lambda} \quad (4.2)$$

therefore, the radiative near field region of the directional antenna is more than or equal to 3.6 cm (0.036 m) but less than or equal to 9 cm (0.09 m).

Finally, the far field region is where the electromagnetic fields are dominated by the radiating fields and hence, the E-fields and H-fields are completely orthogonal to each other and to the

direction of propagation as with plane waves [26] It is denoted in equation (4.3)

$$\text{Far Field Region} \geq \frac{2D^2}{\lambda} \quad (4.3)$$

hence, the far field region of the directional antenna is more than or equal to 9 cm (0.09 m).

4.2 Experiment Setup and Tasks

4.2.1 System Setup

The Wi-Fi Node Measurement System comprises of three essential components which are the Wi-Fi Nodes that refer to the SparkFun ESP32 Thing Board and Directional Antenna, Wi-Fi Router and Remote PC where the data is being collected from the Server. In addition, the Remote PC is used to further process the data collected. Fig. 4.4 displays the block diagram of the constituents of the Wi-Fi Node Measurement System.

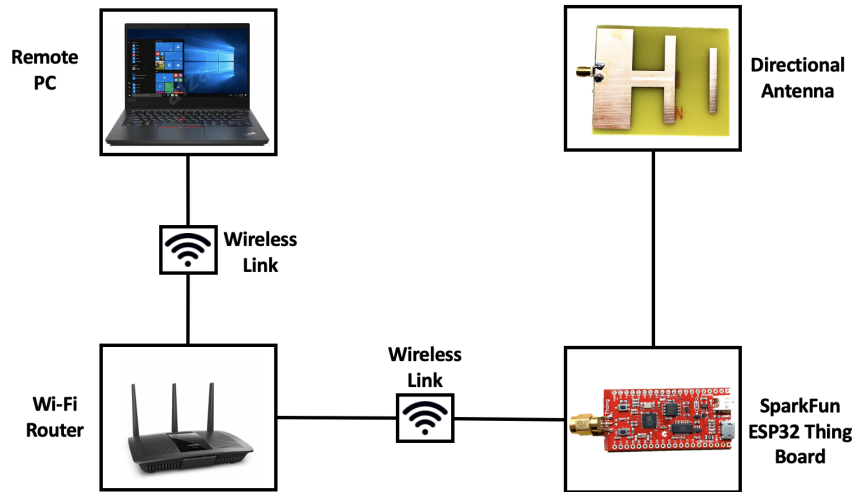


Figure 4.4: Block diagram of the Wi-Fi Node Measurement System.

In order to configure the Wi-Fi nodes, firstly, we have to attach the Directional Antenna with the SparkFun ESP32 Thing Board. Using a micro USB socket, we connect the ESP32 board to a Laptop or PC where the Arduino platform is utilized. With the code written in Visual C++ [24], it

is uploaded and compiled into the ESP32 board by the Arduino IDE. Since we will be using many ESP32 boards, it is important to set each individual board with a distinct and desired board number. In addition, since the ESP32 boards act as the client, the client-side code comprises of switch case statement to handle the Wi-Fi events and errors [24].

Each ESP32 board is running in AP and STA mode thus making it simultaneously connected to a Wi-Fi Router while also acting as its own AP. Passive scanning is taking place when the ESP32 boards perform a Wi-Fi scan because active scanning with a large number of ESP32 boards will cause the ESP32 boards to crash due to the large number of probe requests from all the node APs [24]. The ESP32 board will scan the entire area for APs with the SSID that contains the keyword "Measure" as this represents that another ESP32 board is present. There is a one second delay between the scans in order to prevent the other ESP32 boards from being overloaded by the scans and also to ensure that the ESP32 board itself is not overheated. Once the scan has been completed, the SSIDs and the RSSI for each individual unique SSID is stored in an array and sent to the Server through the AP as a station by using the UDP.

The Wi-Fi Router has its own SSID name and password. All the ESP32 nodes are set to channel 11 and scanning is restricted to channel 11 only in order to enhance the speed. Therefore, even the Wi-Fi Router is also set to channel 11. Finally the Wi-Fi Router is bounded to the MAC address of the Server (Remote PC) through the IP Address of 192.168.0.118.

From the Remote PC side, the Server has been established and programmed in the Python language [24]. The Server code is executed in the Remote PC terminal and the data from the ESP32 boards is received by the Remote PC where it is processed and stored as a log file. The log file comprised of the ESP32 board from which the data was broadcasted from, the SSID and the corresponding RSSI of the other ESP32 boards that were discovered [24]. The Server itself then orders the array as there is no particular order in which the SSIDs are sent. The data is collected and stored in new .txt file every 60 minutes. The sample title of filename is as following "log - (0000hrs-10-02-2019).txt" whereby the date is in the format of Day-Month-Year. These files are stored in individual directories that have a sample format title of "Year-Month-Date-Hour-Minute-Second" as this allowed us to keep track of the time when the system was being operated for collecting the data while performing the experiment. In addition, Once the raw data has been collected, code has

been written in MATLAB to further process the raw data in order to obtain the reconstruction and imaging results.

4.2.2 Experimental Tasks and Procedures

Once the system setup has been completed, the next major focus is explain the different experiments that we have conducted.

In the first experiment, we decided to use two ESP32 boards and placed face to face and positioned them at a variety of distance between them with the starting distance of separation being 0.5 m with an increment of 0.5 m and ending distance being 5 m. Fig. 4.5 shows an example of two ESP32 boards placed opposite to each other.



Figure 4.5: Two ESP32 boards placed apart from each other.

The aim of this experiment is to firstly determine the change in mean and standard deviation of the RSSI levels at different distances of separation. This will allow us to determine a suitable distance threshold such that increasing the distance of separation does not produce a significant change with regards to the RSSI levels. In addition, we will be comparing the mean of the RSSI levels with the two-ray ground reflection model.

Subsequently, the second experiment focused on again using two ESP32 boards that are placed 3 m apart and we decided to introduce objects with wide range of permittivities such as human being and furniture like table. This will allow us to determine the change in the RSSI level between two ESP32 boards and detect the presence and/or absence of the physical object.

Finally, in the third experiment, we utilized the 20 ESP32 boards that have been developed, we plan to have the sensor arrangement identical to the one in Fig. 3.3. We examined the RSSI levels of any of the two combination of ESP32 boards with regards to the time in order to understand the different range of RSSI levels being received by the ESP32 board at different locations. Afterwards, we can collect the RSSI data for ten minutes in the 3 m by 3 m region with different types of situation that are:

- Empty region with no physical object present
- Presence of one human
- Presence of two humans

Fig. 4.6 displays the 3 m by 3 m region that has been designed to conduct the experiment with 20 ESP32 boards placed.

4.3 Two-Ray Ground-Reflection Model

Before presenting the results, it is essential to understand the importance of the two-ray ground-reflection model. The two-ray model is a propagation model that has been used extensively to explain the multi-slope behaviour of observed path loss [27] and predicts the path loss between a transmitting antenna and receiving antenna that are usually present at different height. In addition, this model takes into account the effect of the reflections from the ground and its impact on the received signal. This model is displayed in Fig. 4.7 [28].

Reflection coefficient R characterizes the ground surface as it depends on the properties of the material of the surface and type of wave polarization. In addition, the transmitting and receiving antennas have height of h_t and h_r respectively with the distance of separation being d meters [28].



Figure 4.6: 20 ESP32 boards placed around the surrounding of a 3 m by 3 m region.

The received signal comprises of two essential components which are the LOS ray that propagates through the free-space from the transmitter and also a reflected ray from the ground. The distances traveled by the LOS and reflected ray are show in expression (4.4) [28].

$$\begin{aligned} d_{los} &= \sqrt{d^2 + (h_t - hr)^2} \\ d_{ref} &= \sqrt{d^2 + (h_t + hr)^2} \end{aligned} \quad (4.4)$$

The phase difference between the LOS ray and reflected ray can be denoted as ϕ as the received signal may have an impact from constructive or destructive interference. Therefore, the interference model can be expressed in equation (4.5)

$$\phi = \frac{2\pi(d_{ref} - d_{los})}{\lambda} \quad (4.5)$$

λ is the wavelength of the radiating wave determined from the transmitting frequency [28]. Henceforth, the power of the received signal can be denoted as in equation (4.6).

$$P_r = P_t \left[\frac{\lambda}{4\pi} \right]^2 \left| \frac{\sqrt{G_{los}}}{d_{los}} + R \frac{\sqrt{G_{ref}} \exp(-j\phi)}{d_{ref}} \right| \quad (4.6)$$

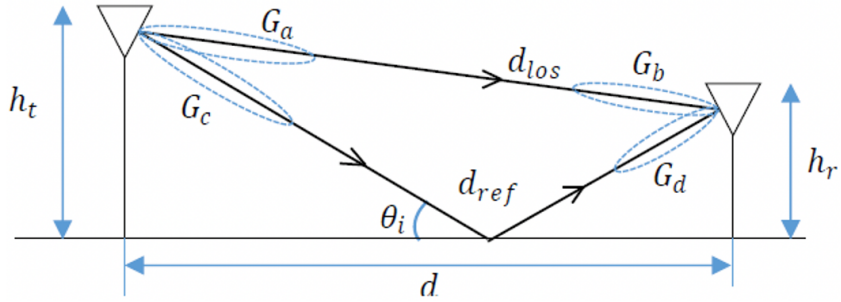


Figure 4.7: Two-ray ground-reflection model.

whereby P_r is the receiving power, P_t is the transmitting power. $\sqrt{G_{los}} = \sqrt{G_a G_b}$ represents the product of the antenna field patterns along the LOS direction meanwhile, $\sqrt{G_{ref}} = \sqrt{G_c G_d}$ represents the product of the antenna field patterns along the reflected path as shown in Fig. 4.7 [28].

4.4 Experimentation Results

4.4.1 Results of Experiment One and Two-Ray Ground-Reflection Model Simulations

For experiment one, we performed four trials for this experiment and across multiple days to ensure that we were receiving consistent results. Fig. 4.8 displays the mean RSSI that has been obtained between the two ESP32 boards that were placed apart from each other at an increment of 0.5 m with the starting distance of 0.5 m and ending distance of 5 m. Fig. 4.9 displays the standard deviation of the RSSI across different distances of the multiple trials performed.

Based on Fig. 4.8, we can see that there is a decrease in the RSSI as the distance of separation increases and the trend is similar across all the four trials performed. Fig. 4.9 shows the standard deviation of the RSSI is less than 1 dBm which is quite exceptional thus suggesting that the implementation of the directional antenna has reduced the impact of multipath fading and there is less disturbance in the RSSI reading.

After having an understanding of the two-ray ground-reflection model, we can modify equation

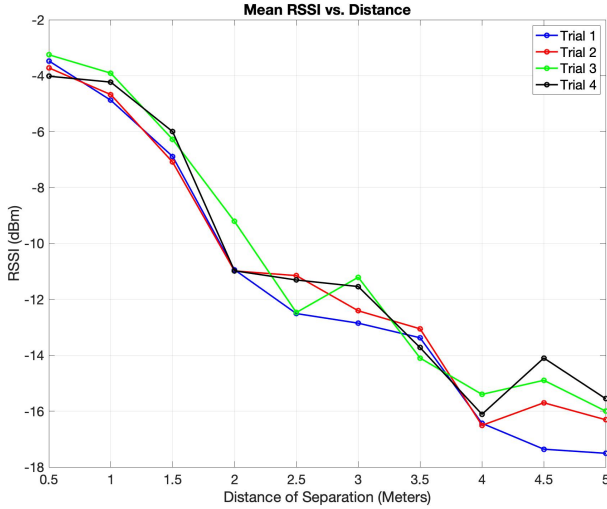


Figure 4.8: Mean RSSI obtained between two ESP32 boards placed apart from each other at an increment of 0.5 m. Four trials were performed across multiple days.

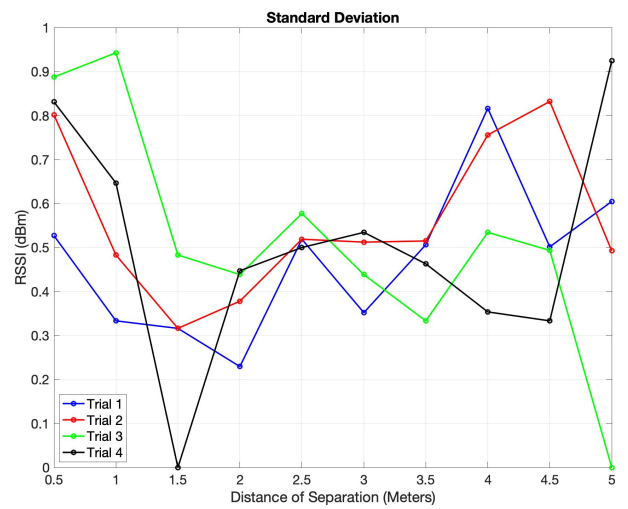


Figure 4.9: Standard deviation of the RSSI obtained between two ESP32 boards placed apart from each other at an increment of 0.5 m. Four trials were performed across multiple days.

(4.6) to take into account the gain or directivity of both the two ESP32 boards that are acting as transmitting and receiving antenna. Equation (4.7) represents the modified two-ray ground-reflection model equation

$$P_r = P_t D_t D_r \left[\frac{\lambda}{4\pi} \right]^2 \left| \frac{1}{d_{los}} + R \frac{\exp(-j\phi)}{d_{ref}} \right| \quad (4.7)$$

whereby D_t is the directivity (gain) of the transmitting antenna, D_r is the directivity (gain) of the receiving antenna. The transmitting power of the ESP32 board P_t has been set to 19.5 dBm. Meanwhile, G_{los} and G_{ref} are equivalent to 1 and thus considered negligible. In the case of our experimentation, λ of Wi-Fi signal of 2.4 GHz is 0.125 m. The height at which the two ESP32 boards are placed at a height of 1.2 m on a wooden stick hence, both h_t and h_r is equivalent to 1.2 m. d_{los} and d_{ref} can be obtained from equation (4.4). The value of D_t and D_r is 6.6 dBi and for the reflection coefficient R , we will be using four values of 0, $-\frac{1}{4}$, $-\frac{1}{2}$ and, -1 in order to make comparisons. Fig. 4.10 is a simulation of the modified two-ray ground-reflection model from equation (4.7) with the different values of reflection coefficient R . Fig. 4.11 shows the comparison of the mean RSSI results obtained from experiment one along with the two-ray ground-reflection model.

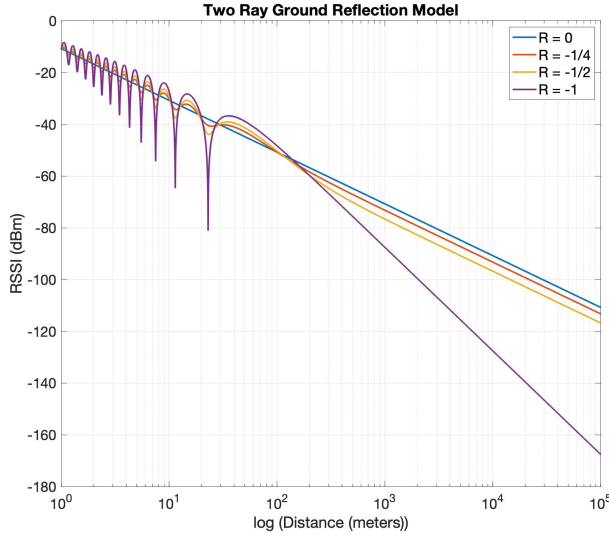


Figure 4.10: Simulation of two-ray ground-reflection model with consideration of directional antenna directivity and wide range of reflection coefficient R .

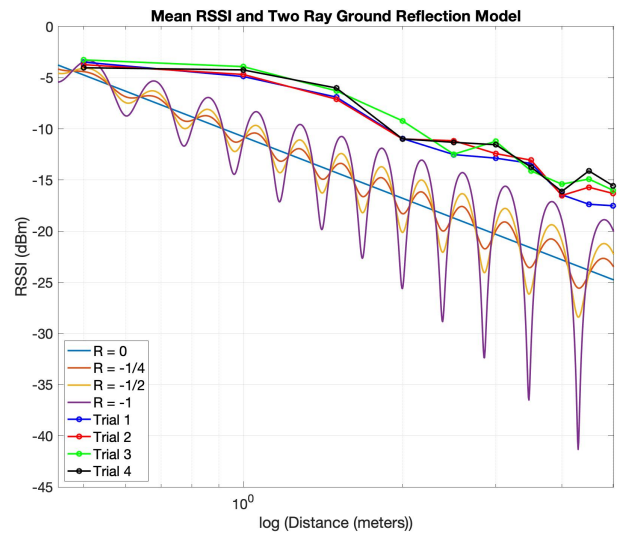


Figure 4.11: Comparison of the simulation of the two-ray ground-reflection model with the mean RSSI results of experiment one from the different trials performed.

Based from Fig. 4.10, we can see that given that h_t and h_r are equivalent, the LOS ray and reflected ray are adding up constructively and destructively thus giving us with regions of upward and downward fades in RSSI. As the distance increases beyond the critical distance and R being equivalent to -1 , it can be seen that the RSSI is dropping proportionally to an inverse of the fourth power of the distance. Meanwhile, it can be observed that when R is equal to 0 , the two-ray ground-reflection model is equivalent to the free-space path loss. The free-space path loss is the received signal between two antennas in the LOS path through free-space and is denoted in expression (4.8)

$$P_r = P_t D_t D_r \left(\frac{\lambda}{4\pi d} \right)^2 \quad (4.8)$$

hence, for R equal to 0 , $-\frac{1}{4}$ and, $-\frac{1}{2}$, we can that as the distance increases beyond the critical distance, the RSSI is dropping proportionally to an inverse of the second power of the distance. In addition, as the value of R increases and becomes closer to 0 , the amplitude of the RSSI begins to decrease. Based on Fig. 4.11, we can see that the values of mean RSSI from the different trials are decreasing in the same pattern as the two-ray ground-reflection model. There is a small difference present between both the experimental results and two-ray ground-reflection model however, the

slope of four trials of the mean RSSI values matches the slope of the two-ray ground-reflection model when R is equivalent to 0. This further highlights that the directional antenna has reduced the impact of multipath fading.

4.4.2 Results of Experiment Two with Different Objects

After the completion of experiment one, we decided to introduce different objects between the two ESP32 boards. Given that our domain of interest is 3 m by 3 m, we have decided to place the objects at the midpoint (1.5 m) of the two ESP32 boards that are placed 3 m apart. Fig. 4.12 is an image of a wooden table placed between two ESP32 boards and Fig. 4.13 displays the change in the RSSI readings.



Figure 4.12: Wooden table placed between two ESP32 boards.

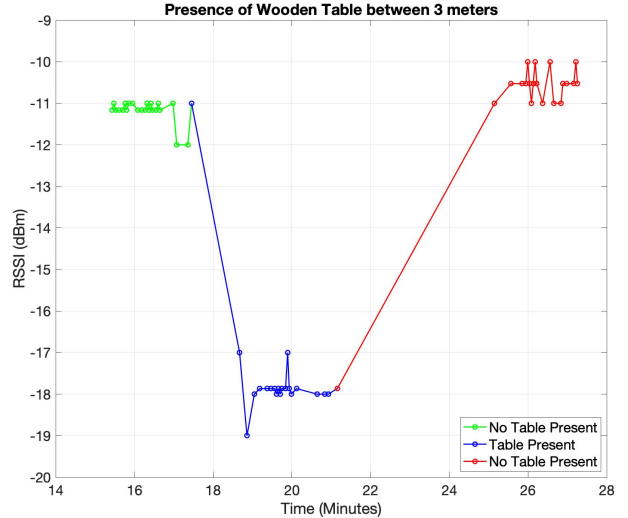


Figure 4.13: Result obtained by placing wooden table between two ESP32 boards.

As seen from Fig. 4.13, we can see that there is a decrease in the RSSI with the RSSI decreasing from around -11 dBm to around -18 dBm. Given that wood has a typical permittivity of around 2 to 6 [21], the decrease in RSSI is a solid indication that presence is of wooden object is causing an interference with the Wi-Fi signal thus resulting in a difference in the reading of the RSSI. Fig. 4.14 is an image of an individual human placed between two ESP32 boards and Fig. 4.15 displays the change in the RSSI readings when one human and two humans are placed between the two ESP32 boards.



Figure 4.14: One human placed between two ESP32 boards.

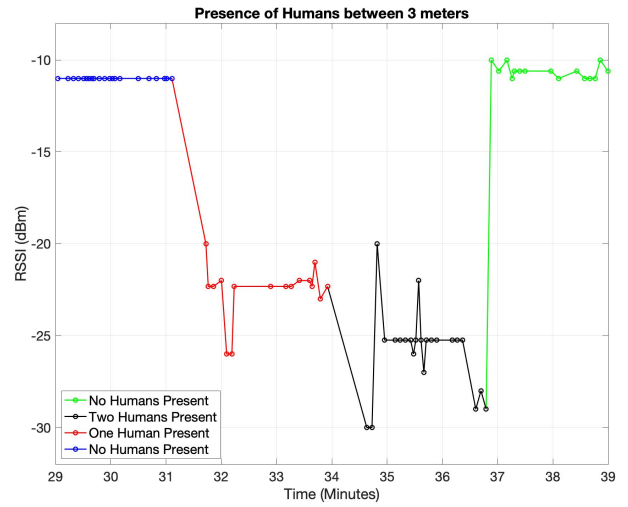


Figure 4.15: Result obtained by placing one and two humans between two ESP32 boards.

Based on Fig. 4.15, we can see that when one human is placed between the two ESP32 boards, there is a change in the RSSI reading from around -11 dBm to around -23 dBm. Similarly, when another human is introduced, the reading drops slightly to around -25 dBm. Since humans have a high water content, the permittivity ranging from 20 to 60 [20] thus causing a much more significant decrease in the RSSI in comparison to the wooden table.

By performing this experiment, we are able to identify that physical objects like wooden furniture and humans would be suitable to reconstruction and localization for experiment three as the introduction of these objects were causing a change (decrease) in the RSSI measurement.

4.4.3 Results from Experiment Three and Imaging Changes within Indoor Environment

Finally, we can commence utilizing 20 ESP32 boards after the completion of experiment two. Fig. 4.16 displays the RSSI readings two randomly chosen ESP32 boards.

As we can see from Fig. 4.16, the implementation of directional antenna has resulted very consistent readings of the RSSI with minimal anomalies. In order to perform imaging, we will be comparing the data of situation to another situation. For example, if we wanted to reconstruct and localize the presence of one human in the domain of interest, we will finding the difference

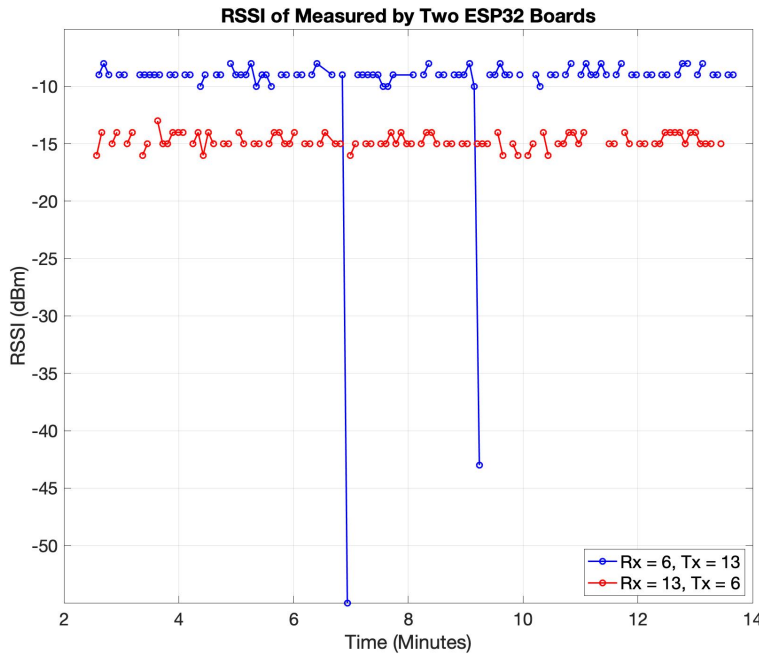


Figure 4.16: RSSI readings between two ESP32 boards numbered 6 and 13. This image shows both situation where board number 6 acts as a transmitter and board numbered 13 acts as a receiver and vice versa.

between the data obtained in the situation when the region is empty with no physical object present and the region when there is a presence of one human. As a result, we will be collecting the data for these individual scenarios for ten minutes and then forming a mode matrix which will eliminate any possibility of anomalies. An example of a mode matrix is shown in Fig. 4.17.

Fig. 4.17 is an example of a mode matrix of the RSSI data obtained after ten minutes of data collection whereby the rows represent the numbered ESP32 boards that are transmitting and the columns represent the numbered ESP32 boards that are receiving the Wi-Fi signals. In theory, the concept of reciprocity is implied that the directional antenna are expected to work equally well for both transmitters and receivers whereby the directional antenna's radiation and receiving patterns are identical. Suppose the reading between two ESP32 boards numbered 6 (transmitter) and 13 (receiver) is -15 dBm, the theory of reciprocity states that the reading between two ESP32 boards numbered 13 (transmitter) and 6 (receiver) should also be -15 dBm. However, in the case of experimentation, there may be occurrences where the readings may not match.

Using our understanding of the mathematics of RTI from Chapter 3 and the data we have col-

	1	2	3	4	5	6	7	8	9	10	11	12	13	14	15	16	17	18	19	20
1	NaN	-6	-14	-20	-22	-9	-9	-9	-10	-11	-11	-16	-15	-11	-10	-13	-19	-10	-14	-6
2	-10	NaN	-25	-31	-33	-20	-17	-20	-14	-18	-22	-17	-16	-11	-8	-13	-17	-17	-10	-7
3	-16	-23	NaN	-19	-21	-14	-12	-9	-8	-13	-13	-12	-11	-11	-10	-13	-13	-12	-10	-9
4	-25	-32	-22	NaN	-22	-14	-14	-13	-15	-22	-19	-17	-16	-15	-16	-18	-18	-16	-20	
5	-22	-32	-19	-18	NaN	-8	-5	-8	-13	-17	-13	-8	-13	-12	-13	-15	-13	-11	-14	-12
6	-13	-19	-16	-12	-11	NaN	-13	-19	-31	-20	-18	-12	-15	-16	-16	-13	-11	-12	-12	-11
7	-9	-13	-11	-8	-5	-10	NaN	-24	-31	-21	-19	-16	-20	-15	-13	-17	-11	-12	-7	-6
8	-9	-15	-7	-8	-8	-15	-23	NaN	-17	-22	-17	-12	-12	-13	-12	-11	-9	-6	-6	-8
9	-12	-12	-8	-11	-15	-32	-32	-20	NaN	-24	-16	-11	-11	-12	-15	-13	-9	-7	-9	-10
10	-12	-15	-12	-17	-17	-17	-21	-22	-21	NaN	-8	-5	-10	-12	-13	-11	-5	-6	-9	-13
11	-12	-19	-12	-15	-13	-15	-20	-19	-15	-10	NaN	-38	-19	-32	-22	-14	-10	-11	-13	-13
12	-22	-19	-16	-17	-13	-13	-22	-18	-14	-7	-40	NaN	-27	-33	-26	-26	-20	-21	-19	-24
13	-12	-10	-8	-8	-10	-9	-17	-10	-7	-8	-16	-19	NaN	-21	-31	-20	-10	-9	-12	-13
14	-13	-8	-10	-11	-13	-13	-16	-14	-11	-13	-32	-30	-28	NaN	-19	-17	-8	-8	-11	-17
15	-11	-6	-9	-11	-14	-14	-14	-14	-14	-16	-23	-23	-34	-19	NaN	-10	-4	-8	-12	-18
16	-13	-9	-11	-12	-14	-9	-16	-11	-11	-10	-12	-20	-22	-16	-9	NaN	-12	-14	-17	-25
17	-22	-16	-15	-16	-16	-11	-14	-13	-10	-8	-12	-18	-16	-9	-5	-15	NaN	-14	-22	-15
18	-13	-16	-13	-13	-14	-11	-14	-9	-8	-8	-13	-19	-14	-9	-9	-18	-13	NaN	-16	-20
19	-17	-9	-12	-14	-16	-11	-10	-9	-10	-12	-15	-17	-13	-13	-21	-22	-17	NaN	-22	
20	-7	-3	-8	-15	-13	-8	-7	-9	-9	-14	-12	-20	-16	-17	-18	-31	-12	-19	-19	NaN

Figure 4.17: Sample of a mode matrix of the RSSI data when there is a presence of one human in the 3 m by 3 m region in the indoor environment.

lected, we can now perform the reconstructions and localization from an experimental point of view. Firstly, we compared the mode matrix data of an empty region with no physical object present with the mode matrix data of one human present in the region. Fig. 4.18 displays an image of a human being present in the 3 m by 3 m region at the coordinate of (1.2, 1.2). Fig. 4.19 displays

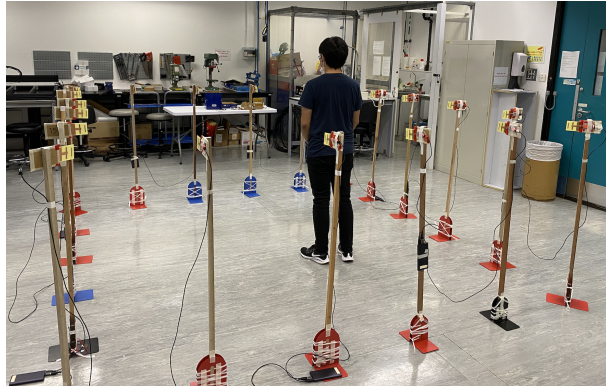


Figure 4.18: One human present in a 3 m by 3 m region in the indoor environment at the coordinate of (1.2, 1.2).

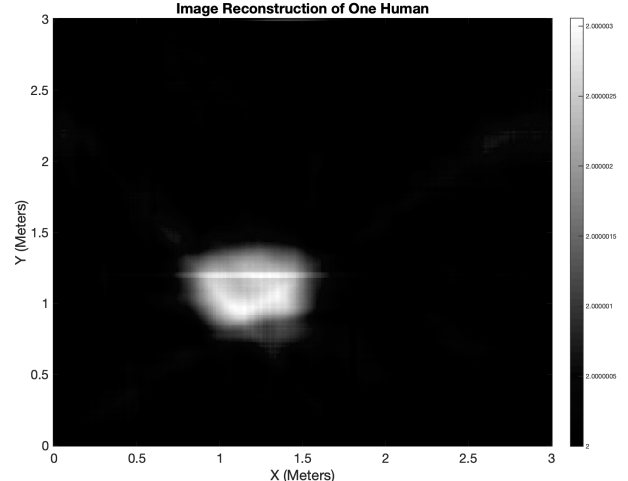


Figure 4.19: Image reconstruction of one human with the localization position being at coordinate of (1.2, 1.2).

the reconstruction of a human being present in the 3 m by 3 m region at the coordinate of (1.2, 1.2) thus suggesting that the 20 ESP32 boards and the LOS based RTI methodology is successfully able to identify the change in the environment and able to detect, model and localize the presence of an object, that being one human at the correct location.

We also decided to test the situation of two humans present in the region. Similarly to the presence of one human in the environment situation, we decided to compare the mode matrix data of an empty region with no physical object present with the mode matrix data of two humans present in the region. Fig. 4.20 displays an image of two human being present in the 3 m by 3 m region with human one being at coordinate (0.6, 1.8) and human two being at coordinate (1.8, 1.2).

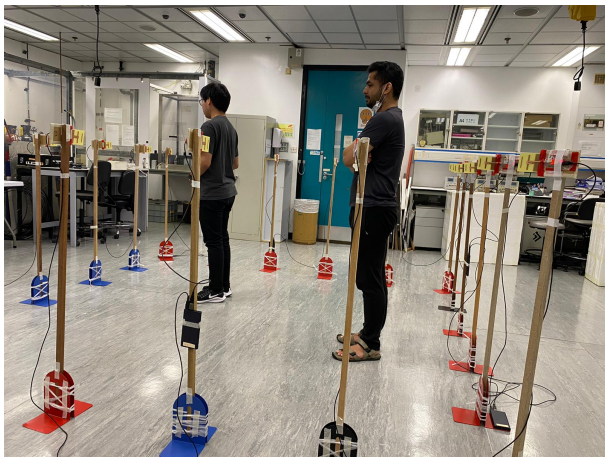


Figure 4.20: Two humans present in a 3 m by 3 m region in the indoor environment with human one being at coordinate (0.6, 1.8) and human two being at coordinate (1.8, 1.2).

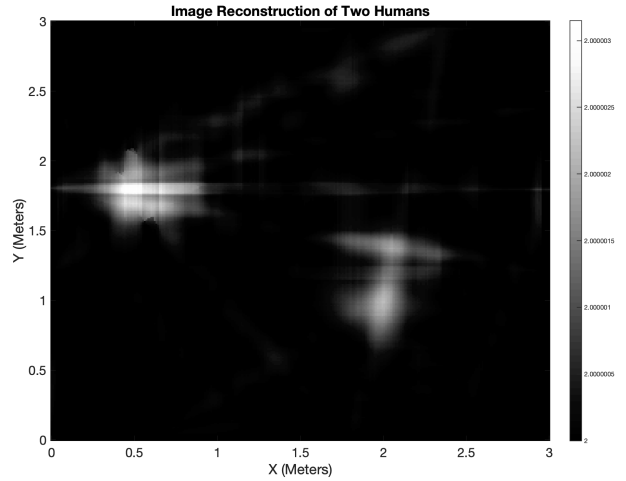


Figure 4.21: Image reconstruction of two human with the localization position of human one being at coordinate of (0.6, 1.8) and human two being at coordinate (1.8, 1.2).

Fig. 4.21 displays the reconstruction of two human being present in the 3 m by 3 m region with human one being at coordinate (0.6, 1.8) and human two being at coordinate (1.8, 1.2).

In order to improve image reconstruction and localization of the experimental results, the results shown in Figs. 4.22 and 4.24 utilize an improved RTI model with 2D total variation-based regularization unlike the previous reconstruction results. The details of the improved model is given in [29].

These image reconstruction and localization results further suggest that our experimentation is also successful at imaging multiple physical objects of high permittivities that are present in the region of the domain of interest.



Figure 4.22: One human present in a 3 m by 3 m region in the indoor environment at the coordinate of (1.2, 1.2).

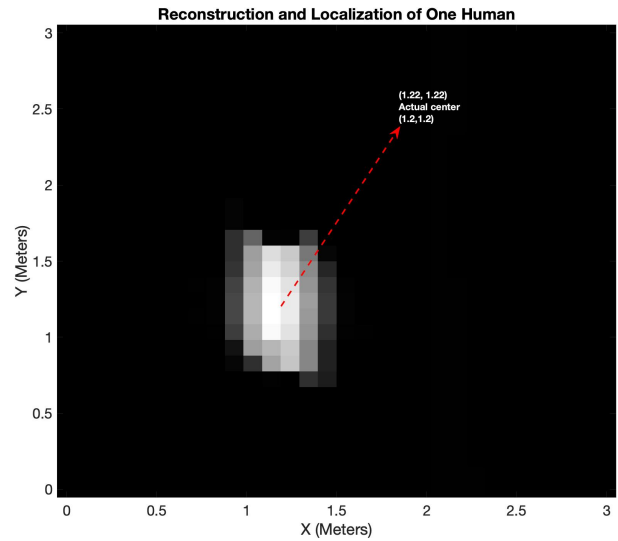


Figure 4.23: Image reconstruction of one human with the localization position being at coordinate of (1.2, 1.2) with the implementation of the improved RTI model.



Figure 4.24: Two humans present in a 3 m by 3 m region in the indoor environment with human one being at coordinate (1.2, 1.2) and human two being at coordinate (2.4, 1.8).

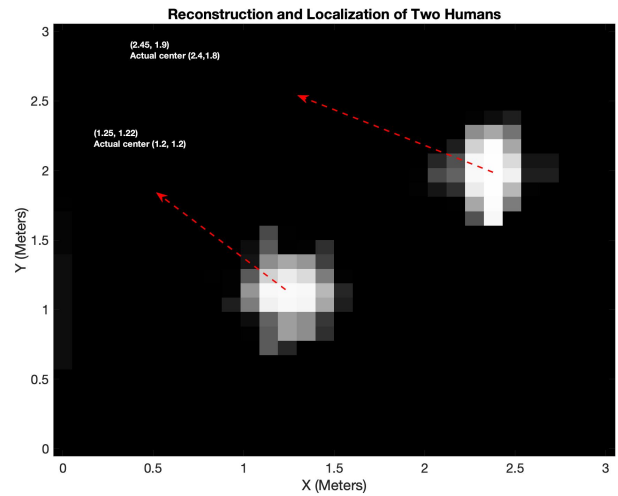


Figure 4.25: Image reconstruction of two human with the localization position of human one being at coordinate of (1.2, 1.2) and human two being at coordinate (2.4, 1.8) with the implementation of the improved RTI model.

CHAPTER 5

CONCLUSION

This thesis has made contributions to the LOS based RTI methodology from both a simulation and experimental perspective. In order to understand the mathematics behind RTI, it was essential to introduce the linear formulation and weight model that would be incorporated into the LOS based RTI model. Subsequently, electromagnetic simulations were performed whereby dielectric cylinders with fixed size and varying permittivities were positioned at certain locations. As a result, we were able to transform these simulations into an inverse problem whereby we examined the least-square-error based solution as approached in [7] and implement the total variation-based regularization which allowed us to examine the reconstruction and localization of the simulated dielectric cylinders at a higher resolution with smaller pixel size. As a result, the total variation-based regularization made it much easier to determine the size of the dielectric cylinder and at which permittivity was the reconstruction successful or failing.

Establishing an experimental setup after deriving the simulations made it possible to add more validity to the simulations that had been obtained. We decided to use inexpensive Wi-Fi hardware modules with directional antenna to design a domain of interest that matched our simulations. Experiments were performed on the Wi-Fi hardware modules with directional antennas by comparing the mean RSSI of two hardware modules with the two-ray ground-reflection model at incremental distances. The simulation made it possible to explore the impact of multipath fading from the ground and its ground reflection coefficient on the RSSI measured by the two hardware modules. In addition, we also decided to introduce physical objects between the two hardware modules to see the interference it caused on the Wi-Fi signal and changes in the RSSI measurements. With the success of this experiment, we were confident to use all the hardware modules to develop a region and place physical objects in it at different coordinates. Through the fundamentals of LOS based RTI model, we were actually able to get reconstructions and accurate localization of physical objects through experimentation.

In addition, the thesis reviews the inverse scattering problem which describes the physics behind the electromagnetic waves and the fundamentals of imaging three-dimensional (3D) objects into two-dimensional (2D) images. This allowed us to explore both the Born and Rytov Approximations and its application in through-wall imaging. These approximations take into account the magnitude and phase of the field (measurements) and we tested these approximations on a wide range of cylinders with different radius and refractive indexes in order to find the limitations of both these approximations.

In summary, the two main contributions of this thesis are as follows:

1. Perform electromagnetic simulations to generate dielectric cylinders with fixed radius and wide range of permittivities in order to reconstruct and localize the position of the cylinder at high resolution through total variation-based regularization.
2. Develop an experimental setup similar to simulation with inexpensive Wi-Fi hardware modules with directional antenna to ensure that physical objects present in the region at different coordinates can be reconstructed and localized.

It is also important to note down that there are still many challenges that need to be addressed for future study.

Firstly, given that we have only performed the experimentation with 20 Wi-Fi hardware modules, we can also look into the possibility implementing more Wi-Fi hardware modules which would increase amount of data we would have for a possibility of obtaining a much more accurate reconstruction and localization image of the physical object that is present in the region. Furthermore, the LOS based RTI model performs well in localization for permittivities greater than 3. This is because the shadowing loss dominates the RSSI and useful location information can be found. When permittivity is less than 3, the LOS model is poor and RTI performs poorly thus being a drawback of this methodology. In addition, this model requires only magnitude (power) measurements of the Wi-Fi signal and does not take into account phase measurements at all. From an experiment point of view, it is also quite difficult to gather phase measurements from the inexpensive Wi-Fi hardware modules. With this being one drawback of the model, there is also a possibility of further exploring the inverse scattering techniques as not only does it model multipath effects due to

scattering of signals, it also takes into account the magnitude and phase measurements of signal. In addition, given that we know that Rytov approximation works well for low refractive index for small and large objects, there is a possibility of exploring a combination of LOS based RTI and Rytov approximation model that is combining the best of both these models in order to obtain reconstructions and localization of physical objects of both small and large sizes with a range of low to high permittivity.

REFERENCES

- [1] D. Yu, Y. Guo, N. Li, and D. Fang, “Dictionary Refinement for Compressive Sensing Based Device-Free Localization via the Variational EM Algorithm,” *IEEE Access*, vol. 4, pp. 9743–9757, 2016.
- [2] J. Hong and T. Ohtsuki, “Device-Free Passive Localization from Signal Subspace Eigenvectors,” in *2014 IEEE Global Communications Conference*, pp. 430–435, Dec 2014.
- [3] Q. Lei, H. Zhang, H. Sun, and L. Tang, “Fingerprint-Based Device-Free Localization in Changing Environments Using Enhanced Channel Selection and Logistic Regression,” *IEEE Access*, vol. 6, pp. 2569–2577, 2018.
- [4] Liu Heng, Wang Zheng-huan, Bu Xiang-yuan, and An Jian-ping, “Image Reconstruction Algorithms for Radio Tomographic Imaging,” in *2012 IEEE International Conference on Cyber Technology in Automation, Control, and Intelligent Systems (CYBER)*, pp. 48–53, May 2012.
- [5] C. Alippi, A. Mottarella, and G. Vanini, “A RF map-based localization algorithm for indoor environments,” in *2005 IEEE International Symposium on Circuits and Systems (ISCAS)*, pp. 652–655 Vol. 1, May 2005.
- [6] R. K. Martin, C. Anderson, R. W. Thomas, and A. S. King, “Modelling and Analysis of Radio Tomography,” in *2011 4th IEEE International Workshop on Computational Advances in Multi-Sensor Adaptive Processing (CAMSAP)*, pp. 377–380, Dec 2011.
- [7] J. Wilson and N. Patwari, “Radio Tomographic Imaging with Wireless Networks,” *IEEE Transactions on Mobile Computing*, vol. 9, pp. 621–632, May 2010.
- [8] S. Depatla, L. Buckland, and Y. Mostofi, “X-ray Vision With Only Wifi Power Measurements Using Rytov Wave Models,” *IEEE Transactions on Vehicular Technology*, vol. 64, pp. 1376–1387, April 2015.

- [9] M. Slaney and A. C. Kak, “Diffraction Tomography,” in *Inverse Optics I* (A. J. Devaney, ed.), vol. 0413, pp. 2 – 19, International Society for Optics and Photonics, SPIE, 1983.
- [10] A. C. Kak and Malcolm Slaney, *Principles of Computerized Tomographic Imaging*. IEEE Press, 1972.
- [11] P. Müller, M. Schürmann, and J. Guck, “The Theory of Diffraction Tomography,” 07 2015.
- [12] R. Bates, V. Smith, and R. D. Murch, “Manageable multidimensional inverse scattering theory,” *Physics Reports*, vol. 201, no. 4, pp. 185–277, April 1991.
- [13] K. Barkeshli and S. Khorasani, *Approximate Methods*, pp. 337–344. Cham: Springer International Publishing, 2015.
- [14] S. Depatla, C. R. Karanam, and Y. Mostofi, “Robotic Through-Wall Imaging: Radio-Frequency Imaging Possibilities with Unmanned Vehicles,” *IEEE Antennas and Propagation Magazine*, vol. 59, pp. 47–60, Oct 2017.
- [15] S. Soro and W. Heinzelman, “A Survey of Visual Sensor Networks,” *Advances in Multimedia*, vol. 2009, 06 2009.
- [16] C. Alippi, M. Bocca, G. Boracchi, N. Patwari, and M. Roveri, “RTI Goes Wild: Radio Tomographic Imaging for Outdoor People Detection and Localization,” *IEEE Transactions on Mobile Computing*, vol. 15, July 2014.
- [17] M. Ajmani, S. Sinanović, and T. Boutaleb, “Optimal beam radius for LED-based indoor positioning algorithm,” in *2016 International Conference for Students on Applied Engineering (ICSAE)*, pp. 357–361, Oct 2016.
- [18] O. R. Popoola, W. O. Popoola, R. Ramirez-Iniguez, and S. Sinanović, “Optimization of Duty Cycles for LED based Indoor Positioning System,” in *2016 International Conference for Students on Applied Engineering (ICSAE)*, pp. 368–372, Oct 2016.
- [19] B. M. Beck, J. H. Kim, R. J. Baxley, and B. T. Walkenhorst, “RadioBOT: A Spatial Cognitive Radio Testbed,” in *2013 IEEE Aerospace Conference*, pp. 1–9, March 2013.

- [20] E. Aguirre, J. Arpon, L. Azpilicueta, S. D. Miguel Bilbao, V. Ramos, and F. Falcone, “Evaluation of Electromagnetic Dosimetry of Wireless Systems in Complex Indoor Scenarios with Human Body Interaction,” *Progress In Electromagnetics Research B*, vol. 43, pp. 189–209, 09 2012.
- [21] Jemai, Kumer, Varone, and Wagen, “Determination of the Permittivity of Building Materials through WLAN Measurements at 2.4 GHz,” in *2005 IEEE 16th International Symposium on Personal, Indoor and Mobile Radio Communications*, vol. 1, pp. 589–593, Sep. 2005.
- [22] X. Chen, *Computational Methods for Electromagnetic Inverse Scattering*. Wiley Online Library, 2018.
- [23] S. Boyd and L. Vandenberghe, *Convex Optimization*. Cambridge university press, 2004.
- [24] R. D. Murch, “Multiple Wi-Fi Node Measurement System,” pp. 1–6, February 2019.
- [25] “ESP32 Thing Hookup Guide.” <https://learn.sparkfun.com/tutorials/esp32-thing-hookup-guide>. Accessed: 2020-06-20.
- [26] “What are Near Field and Far Field Regions of an Antenna?” <https://www.everythingrf.com/community/what-are-near-field-and-far-field-regions-of-an-antenna>. Accessed: 2020-06-20.
- [27] E. Zöchmann, K. Guan, and M. Rupp, “Two-Ray Models in mmWave Communications,” in *2017 IEEE 18th International Workshop on Signal Processing Advances in Wireless Communications (SPAWC)*, pp. 1–5, 2017.
- [28] M. Viswanathan, “Two ray ground reflection model.” <https://www.gaussianwaves.com/2019/03/two-ray-ground-reflection-model/>, 2019. Accessed: 2020-06-20.
- [29] A. Dubey, P. Sood, J. Santos, C. Y. Chiu, and R. Murch, “Imaging Changes in Indoor Environment using Approximate Inverse Scattering Method and Wi-Fi Signals.” In preparation.